# Improved compressed sensing algorithm for sparse-view CT

A Thesis Submitted to the College of

Graduate Studies and Research

In Partial Fulfillment of the Requirements

For the Degree of Master of Science

In the Department of Electrical and Computer Engineering

University of Saskatchewan

Saskatoon, Saskatchewan

By

**Zangen Zhu**

# Permission to Use

In presenting this thesis in partial fulfilment of the requirements for a Postgraduate degree from the University of Saskatchewan, I agree that the Libraries of this University may make it freely available for inspection. I further agree that permission for copying of this thesis in any manner, in whole or in part, for scholarly purposes may be granted by the professor or professors who supervised my thesis work or, in their absence, by the Head of the Department or the Dean of the College in which my thesis work was done. It is understood that any copying or publication or use of this thesis or parts thereof for financial gain shall not be allowed without my written permission. It is also understood that due recognition shall be given to me and to the University of Saskatchewan in any scholarly use which may be made of any material in my thesis.

Requests for permission to copy or to make other use of material in this thesis in whole or part should be addressed to:

Head of the Department of Electrical and Computer Engineering

57 Campus Drive

University of Saskatchewan

Saskatoon, Saskatchewan, Canada

S7N 5A9

# Acknowledgements

I would like to thank my supervisors, Khan Wahid and Paul Babyn, for introducing me to the field of computed tomography, and their valuable academic guidance, financial support and encouragement during the work, and their great attitude. The numerical experiments in this thesis rely on the design of reconstruction algorithms. Dr. Wahid and Dr. Babyn helped me a lot in the design of the experiments. Two years studying under their direction is an invaluable experience that will benefit me throughout my life. I also wish to thank Dr. Cooper and his student, Isaac Pratt, Dr. James, for having shared their works and data. I also want to thank Canadian Light Source for providing the equipment to collect data.

It is my fortune to have Professor Anh van Dinh, Francis Bui and Artur Sowa on my thesis committee. I am very grateful for their instructive comments and suggestions.

I wish to express my gratitude to my family for their understanding and support.

Finally, I want to acknowledge funding supports from my supervisors, University of Saskatchewan, and Natural Sciences and Engineering Research Council of Canada (NSERC) and research data from Dr. James of Small Animal Clinical Sciences.

# Abstract

In computed tomography (CT) there are many situations where reconstruction may need to be performed with sparse-view data. In sparse-view CT imaging, strong streak artifacts may appear in conventionally reconstructed images due to the limited sampling rate, compromising image quality. Compressed sensing (CS) algorithm has shown potential to accurately recover images from highly undersampled data. In the past few years, total variation (TV)-base compressed sensing algorithms have been proposed to suppress the streak artifact in CT image reconstruction. In this paper, we formulate the problem of CT imaging under transform sparsity and sparse-view constraints, and propose a novel compressed sensing-based algorithm for CT image reconstruction from few-view data, in which we simultaneously minimize the $\ell_1$ norm, total variation and a least square measure. The main feature of our algorithm is the use of two sparsity transforms: discrete wavelet transform and discrete gradient transform, both of which are proven to be powerful sparsity transforms. Experiments with simulated and real projections were performed to evaluate and validate the proposed algorithm. The reconstructions using the proposed approach have less streak artifacts and reconstruction errors than other conventional methods.

# Table of contents

# List of Tables

# List of Figures

# List of abbreviations

ART: Algebraic Reconstruction Technique

CC: Correlation Coefficient

CS: Compressed Sensing

CT: Computed Tomography

FBP: Filtered Backprojection

FDK: Feldkamp-Davis-Kress

FFT: Fast Fourier Transform

FOV: Field Of View

MRI: Magnetic Resonance Imaging

OMP: Orthogonal Matching Pursuit

ROI: Region Of Interest

RRMSE: Relative Root Mean Square Error

SART: Simultaneous Algebraic Reconstruction Technique

SI: Streak Indicator

SSIM: Structural Similarity

TV: Total Variation

# Chapter 1

# Introduction

X-ray computed tomography (CT) is one of the most popular clinical imaging modalities. It was first introduced by Cormack[1] and Hounsfield[2]. Since the discovery, CT scanners have undergone many developments, including improvements in image reconstruction technique and radiation issues, etc.

## 1.1 Image reconstruction

The measurements obtained from a CT scanner are a series of projection data. Each projection is taken at an angle. The image reconstruction process is to estimate the attenuation density function, $\mu(x,y)$, from these measurements. Filtered backprojection (FBP) is the most dominant CT reconstruction algorithm, which was first developed based on the Radon transform and Fourier slice theorem. Its practical implementation takes advantage of the fast Fourier transform (FFT). It is therefore, analytic, fast and deterministic and available on all commercially available clinic CT scanners.

Algebraic reconstruction technique (ART), an alternative to FBP, can be used to iteratively solve the reconstruction problems [3-6]. The ART algorithm consists of updating the value of each pixel so that the ray sum of the pixels matches the

corresponding element of the measured projection data. In each iteration, the current guess of the image is re-projected and checked to see how it matches with the real measurements. ART is a geometry free reconstruction algorithm and thus can be applied to any CT scanner. However, it requires large amounts of memory to store data[7]. However increases in computing power may render them more available over time. Today, several variants of ART are also available[8, 9]. Detailed discussion about these algorithms is given in the following chapters.

## 1.2 Motivation

The use of CT examination has increased a lot since 1980s. However, by its nature, CT is considered as a radiation-intensive procedure. The increased use of CT examination has brought worldwide concern to the risk of developing cancer later in life. For example, in the mid-1990s of US, CT scans contributed to 40% of the collective radiation dose while they regarded only 4% of the total X-ray procedures[10]. Within the US in 2007 over 69 million scans were obtained, compared with only 2 million scans in 1980[11, 12]. Brenner and Hall [13] estimated that 2% of all cancers in US may be caused by the radiation from CT examination. It is clear that reducing the radiation dose from CT is critical. Additionally, medical research makes extensive use of CT for pre-clinical studies on the microscopic scale, known as micro-CT. Longitudinal studies on experimental

animals such as rats, mice, and rabbits are also restricted in resolution and image quality by radiation dose.

Extensive ongoing efforts have been made to solve the problem of CT radiation dose. Many schemes have been proposed in the literature. One approach to lower the total x-ray radiation dose is to simply reduce the dose level mAs/view in data acquisition protocols. This approach typically results in an insufficient number of x-ray photons received by the detectors, increasing the noise level on the projection data. The noise-contaminated projection data will degrade the quality of reconstructed CT images when a FBP algorithm is used[14].

Another way to reduce the total radiation dose is to reduce the number of necessary projections, which is usually referred to as few projection problem. By solving this problem we can enhance both the safety and the productivity of a CT system because lower radiation dose and shorter data acquisition time. Unfortunately, according to the standard image reconstruction theory in image processing, when the number of the view angles does not satisfy the Shannon/Nyquist sampling theorem, aliasing artifacts will spread out in the reconstructed images, which can make the accurate reconstruction impossible. As a consequence, the classical FBP algorithms do not produce diagnostically satisfactory images in sparse-view data collection schemes, because they assume the sampled projections over the scanning angular range are dense. Although ART and simultaneous algebraic reconstruction technique (SART) can handle incomplete data sets

better than FBP, they fail to maintain clinically acceptable image quality when the Shannon/Nyquist sampling requirement is seriously violated, i.e., less than 100 view angles compared to 1800 under Nyquist sampling requirement, because the linear system will become highly underdetermined and unstable.

## 1.3 Objectives

In the past few years, compressed sensing (CS) [15-18] algorithms have attracted tremendous attention in the CT and micro-CT community. The idea of CS originated from image compression. In image compression, such as in JPEG[19] and JPEG2000[20], most of the acquired data sample will be eventually discarded as only a small fraction of the coefficients are truly needed. It's therefore natural to investigate a way to avoid acquiring this large amount data before beginning. One may view a CS based algorithm as simply another iterative algorithm, but what makes the CS method distinctive from other iterative algorithms is that it exploits the sampling strategy in which the way the data are sampled truly helpful for an accurate reconstruction of an image object. In other words, it combines data compression with data acquisition. Therefore, no redundant data is acquired. As a result, one can perfectly reconstruct an image with far fewer samples than previously thought.

Putting CS in the context of CT imaging, several CT image reconstruction

algorithms have been already proposed in the sparse-view reconstruction scenario [21-25]. In particular, total variation (TV) based methods have demonstrated their power in CT reconstruction with only a few x-ray projections with their dataset [21-25]. For example, Sidky et. al. demonstrated that their method can yield accurate reconstructions in ideal conditions where only 20 view angles projection data were acquired using simulated data from a jaw phantom[22]. In such algorithms, an objective function of TV norm is minimized subject to a data fidelity posed by the acquired projection data. Minimizing the image gradient essentially suppresses those high spatial frequency components such as streaking artifacts and noise in the image space. The major problem of this TV based compressed sensing method is that it tries to uniformly penalize the image's gradient irrespective of the underlying image structure and thus low contrast regions are sometimes over smoothed[14].

In this thesis, we propose a novel algorithm based on compressed sensing for CT image reconstruction. The algorithm jointly minimizes the wavelet transform and total variation of the object image. Towards that end, we present the following objectives:

- Suppression of streaking artifacts and noise. As total variation minimizes the image gradient, therefore, the streaking artifacts and noise will be greatly reduced in reconstructed images.
- Preservation of detailed information. 2-D wavelet transforms are good at capturing point singularities and small patches [26], thus preserving fine structures and low

contrast information.

- Developing a nonlinear conjugate gradient descent iterative algorithm. Nonlinear conjugate gradient descent algorithm has global convergence and low computational complexity compared to interior point methods. We propose a fast convergent algorithm for solving the image reconstruction problem.

- Reduce the radiation dose. Since the proposed algorithm is based on the theory of compressed sensing, it's able to reconstruct the CT image with fewer x-ray projections than traditional reconstruction methods. As a result, amount of radiation absorbed by patients during CT examinations will be reduced.

- Higher image quality. The proposed algorithm can simultaneously suppress the streaking artifacts, noise and preserving detailed structures, resulting in an improved image.

## 1.4 Organization of Dissertation

This chapter discusses the background and motivation behind the work presented in this thesis. Chapter II provides an introduction to CT by providing a general background on X-ray physics, FBP and iterative image reconstruction methods and image degradation problem. Chapter III presents the mathematical framework of compressed sensing and existing algorithms in CT imaging. Chapter IV presents our algorithm, implementation

and experiments applied on absorbed based CT imaging. We conclude in Chapter V with a summary and an outline for possible extensions of this work.

# Chapter 2

# Introduction to Computed Tomography

This chapter consists of a general introduction to computed tomographic imaging. Firstly, Section 2.1 describes the history, some current trends and properties of X-ray Computed Tomography (CT). The physics of X-ray will be briefly discussed in Section 2.2, including how X-rays are produced, how the X-ray intensity decays when traversing objects. The Radon transform, which is essentially the linear mathematical model of X-ray attenuation, is explained in Section 2.3. Additionally, standard methods to reconstruct the image from its Radon transform are also discussed. Iterative reconstruction techniques will be discussed in Section 2.4. Finally, the factors that cause image degradation are included in Section 2.5.

If the reader is interested in a more in-depth coverage of the subjects, please refer to the work of Kak and Slaney[7], Kalender [27] and Hsieh[28].

## 2.1 History of Computed Tomography

X-ray Computed tomography is an imaging modality that generates cross-sectional images, whose elements correspond to the linear attenuation coefficients of the object. An X-ray tube emits X-ray beams that pass through the slice of interest. The output X-ray

intensity is then measured by a detector on the other side of the object. The output intensity depends on the material distribution of the object. These measurements are called a “view” or a “projection”. This projection process is repeated over some angles. The CT reconstruction is then essentially obtaining an image from these projection data.

The first generation CT scanners were parallel beam scanners. For instance, the original EMI head scanner used a pencil-thin beam. The images were acquired by a way where the X-ray source and the detectors move together around the patient by one degree at one time. The scan time per slice was 4 1/2 minutes with a total rotation of 180 degrees (Figure 2.1).

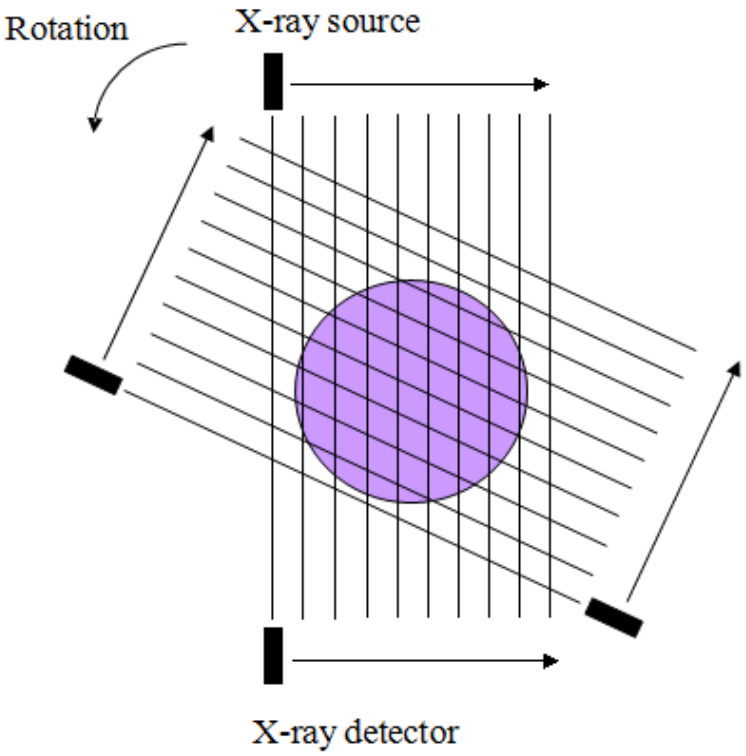


Figure 2.1 First generation CT scanner.

The long scan time associated with parallel beam CT scanner results in low image quality when patient motion can not be ignored. Second generation scanners use partial fan beams. The X-ray source changed from a parallel pencil beam to a fan beam by adding detectors. In this way, several projections could be obtained in a single translation. For example, as depicted in Figure 2.2, if the angle between the pencil beams is 1 degree, then projections from 5 different angles are acquired in a single translation. Consequently, the scan time is reduced by a factor of 5.

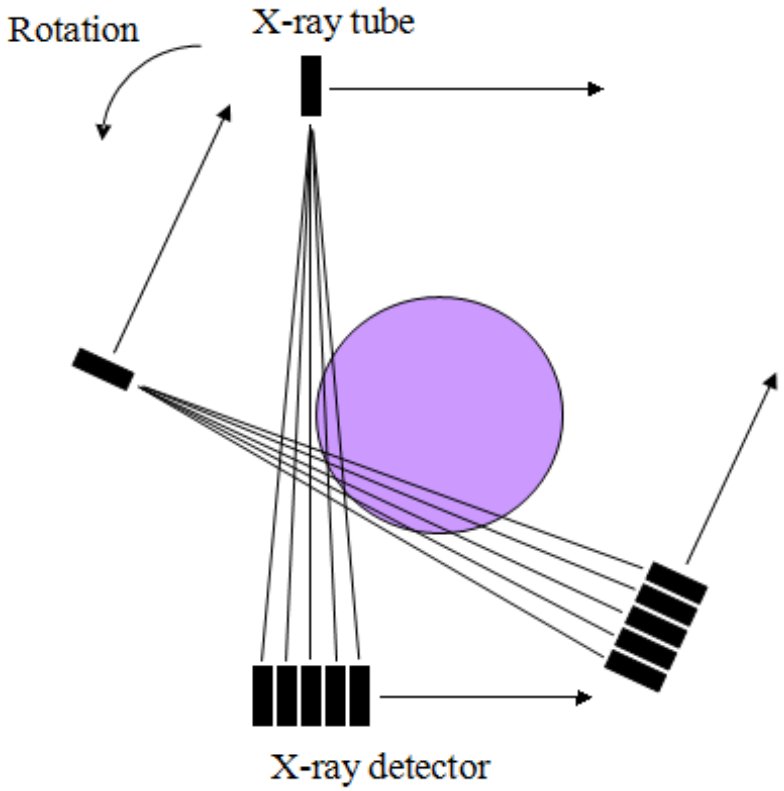


Figure 2.2 Second generation CT scanner. At each instant, measurements from 5 different angles are collected so that the X-ray tube and detector can rotate every 5 degree.

The most popular scanner type is the third generation CT scanner. The array of detectors and the X-ray tube are put in position so that they form a complete arc-shaped

fan beam. And the field of view is large enough to cover the entire slice of interest, see Figure 2.3. By reducing the time of translation, the third generation CT scanner can reduce scan time to less than 10 seconds per slice.

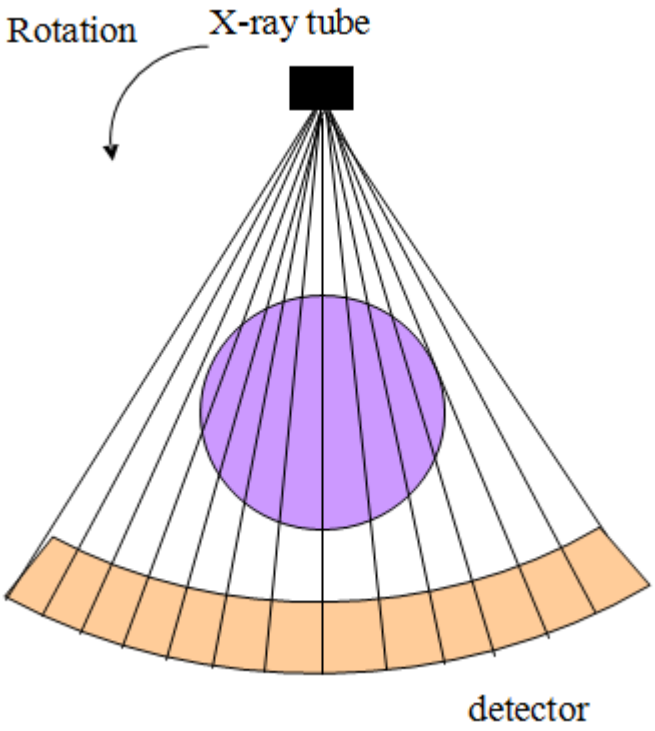


Figure 2.3 Third generation CT scanner.

The fourth generation CT scanner consists of a fixed 360 degree ring of detectors, see Figure 2.4. The advantage of the fourth generation CT scanner is that the data sampling rate is only determined by the rate at which measurements are sampled.

Additionally, another geometry named cone beam CT has been proposed, which is essentially three dimensional. Despite the popularity of cone beam geometry in current X-ray tomography systems, research for parallel beam is highly preferred because the

standard 3D reconstruction is basically a set of weighted 2D reconstructions along tilted planes [29]. Therefore, this thesis will consider 2D parallel geometry.

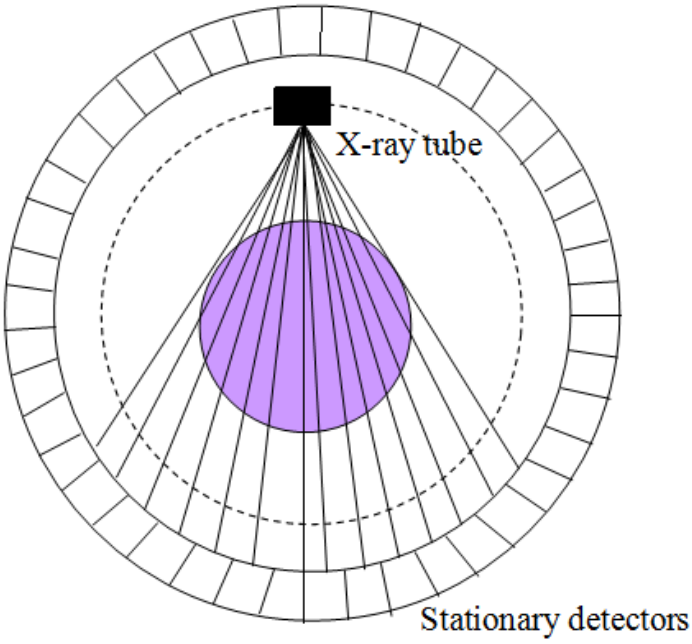


Figure 2.4 Fourth generation CT scanner.

## 2.2 Fundamentals of X-ray Physics

### 2.2.1 Production of X-rays

X-ray is an electromagnetic waveform with a wavelength λ varying from a few picometers ($10^{-3}$ nm) to a few nanometers. The energy of each X-ray photon, $E$, has the following expression:

$$E = \frac{hc}{\lambda} \tag{2.1}$$

where $h$ is Planck's constant and equals $6.63 \times 10^{-34}$ J s, $c$ is the speed of light ($3 \times 10^{8}$ m/s), and $\lambda$ is the wavelength of the X-ray. For convenience, the X-ray energy is usually expressed in units of eV. X-rays with wavelengths in the range of 10 nm to $10^{-3}$ nm correspond to energies from 124 eV to 1.24 MeV respectively.

X-rays are generated in a vacuum tube with a cathode and an anode. By thermal excitation, electrons are released from the cathode. Because of the high voltage between cathode and anode, these electrons are accelerated to a high velocity and eventually collide with a metal target. The majority of these collisions involve ionization of the target atoms by transferring the energy of the high-speed electron to electrons that are knocked out of the atoms, and eventually product heat. In fact, over 99% of the input energy dissipates as heat. The following three types of interactions are of more interest:

- A high-speed electron travels near the nucleus of the atom. The sudden decrease of speed produces so-called bremsstrahlung radiation, emitting a photon. The amount of deceleration (and consequently the energy of the emitted photon) is determined by the distance of the electron to the nucleus. If the electron barely catches the atomic coulomb field, the deceleration is small, resulting in a low-energy photon.
- A high-speed electron interacts with one of the inner-shell electrons of the target atom, which is then liberated from the atom, leaving a vacancy. The hole is filled by an outer-shell electron. Since outer-shell electron has higher energy level, the process

will emit a photon with an energy corresponding to the difference between the binding energies of the two shells. Since in the classic Bohr model of the atom, electrons only occupy orbits with specific quantized energy levels, the emitted photons, as a result, take up only discrete energy values. So this type of X-ray is called “characteristic radiation”.

- A high-speed electron interacts directly with a nucleus and all of its energy is converted to X-ray. The X-ray energy produced by this interaction is the upper limit of possible energies.

For further reading, see [7, 27, 28].

### 2.2.2 X-ray interaction with matter

The linear attenuation coefficient of a material basically depends on both the photon energy and the composition of the material. The two more important types of X-ray interaction with matter in the diagnostic energy range are the photoelectric effect and Compton Effect.

- The photoelectric effect occurs when a tightly bound electron is hit by an X-ray photon with an energy greater than the electron’s binding energy. The entire energy of the X-ray photon is absorbed by the electron and thus the electron is liberated. An outer-shell electron quickly fills the hole left by the ejected electron and emits the so called characteristic radiation. For tissue-like materials and bone materials, the

binding energy is so low that this X-ray photon can not travel very far in tissue. Therefore, we can assume that all the characteristic X-rays produced by the photoelectric effect in the body are absorbed by the patients.

- The most important interaction mechanism for tissue attenuation is Compton scattering where an X-ray photon collides with a bounded electron at a much higher energy than the electron's binding energy. The incident photon is deflected or scattered and gives up part of its energy to free the electron from the atom. The scattered photon may be deflected at any angle varying from 0 to 180 degree. Low energy photons are probably not detected because they are preferentially backscattered (angle from 90 to 180 degrees). On the other hand, high energy photons have a greater probability of being scattered in the forward direction (angle 0 to 90 degrees). Since these high energy photons might undergo several deflections before detected, they provide little spatial information about the interaction.
- The less important type of interaction is the coherent scattering. In this interaction, no electron is released and thus no energy is transformed into kinetic energy. The reader is encouraged to explore the literature for more in-depth description of the interaction mechanisms in [7, 27-30].

The net impact of these interactions is that the photons are either absorbed (photoelectric), scattered (Compton and coherent). Therefore, when the X-ray photons travel through a material such as a patient, they are attenuated. Consider a

monochromatic X-ray beam with incident intensity $I_0$, the attenuation can be expressed by an exponential relationship[28]:

$$I = I_0 e^{-(\mu_p + \mu_c + \mu_r)L} \tag{2.2}$$

where $I$ is the measured intensity of the beam after passing through the object, and $L$ is the thickness of the object. $\mu_p$, $\mu_c$, $\mu_r$ are the attenuation coefficients of photoelectric, Compton and coherent, scattering interactions, respectively. Equation (2.2) is often expressed as the so called Lambert-Beers law[31]

$$I = I_0 e^{-\mu L} \tag{2.3}$$

where $\mu$ is the linear attenuation coefficient of the material.

## 2.3 Analytical image reconstruction method

In this section, we discuss standard methods for the reconstruction of a 2D image slice from one dimensional projections. We present the classical approach: filtered backprojection (FBP), as this is widely used in current clinical practice. The mathematical derivation of FBP is given. For the reason of simplicity, we restrict our discussion to parallel beam CT. Fan beam and cone beam CT require some modifications that are available in[32-34].

### 2.3.1 Radon transform

Equation (2.3) assumes the attenuation coefficients are uniform. When the object has

nonuniform attenuation coefficients, we can divide the object into smaller elements, whose size is sufficiently small so that each element can be considered as uniform. Then equation (2.3) can be rewritten as

$$I = I_0 e^{-\mu_1 \Delta l} e^{-\mu_2 \Delta l} e^{-\mu_3 \Delta l} \cdots e^{-\mu_N \Delta l} = I_0 e^{-\sum_{n=1}^{N} \mu_n \Delta l} \tag{2.4}$$

or

$$-\ln \frac{I}{I_0} = \sum_{n=1}^{N} \mu_n \Delta l \tag{2.5}$$

As $\Delta l$ approaches zero, the above summation becomes the integral over the path

$$p = -\ln \frac{I}{I_0} = \int_L \mu \, dl \tag{2.6}$$

$p$ is the projection measurements in CT.

Let $\mu(x,y)$ denote the x-ray attenuation coefficient distribution of the object we are trying to reconstruct and $p_\theta(t)$ represent the parallel projection of $\mu(x,y)$ taken at an angle θ, as shown in Figure 2.5. By the rotation of coordinate system, the line integration along the ray path is performed by integration along $s$ direction. From equation (2.6), the projection $p_\theta(t)$ can be expressed as

$$p_\theta(t) = \int_l \mu(x, y) dl \tag{2.7}$$

The collection of these $p_\theta(t)$ at all θ forms a 2D image $p_\theta(t)$, which is called sinogram or Radon transform of image $\mu(x,y)$, as shown in Figure 2.6.

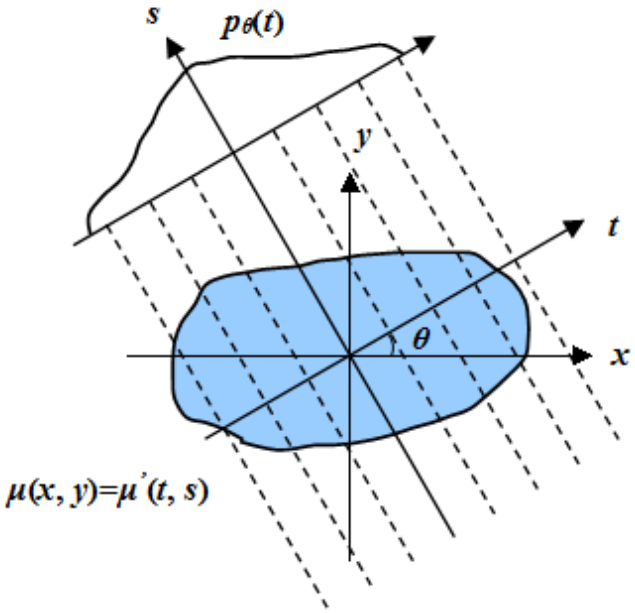


Figure 2.5 Schematic figure of coordinate rotation.

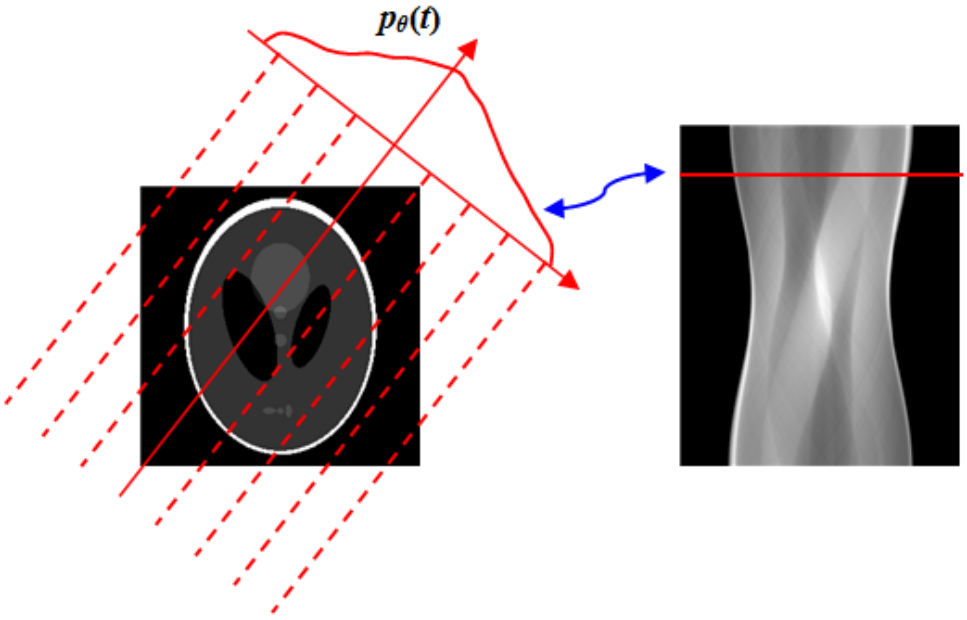


Figure 2.6 Illustration of mapping between image space (left) and sinogram space (right).

A sinogram is formed by putting all projections from different angle views together.

## 2.3.2 Fourier Slice Theorem

The Fourier slice theorem, also known as the central slice theorem, is the fundamental analytical reconstruction technique in tomography. Simply, the theorem states that the one dimensional Fourier transform of a parallel projection of an image $\mu(x,y)$ obtained at angle θ equals a line in a two dimensional Fourier transform of $\mu(x,y)$ taken at the same angle [28, 35].

To derive the Fourier Slice Theorem, one can define the two dimensional Fourier transform $F(u,v)$ of the object $\mu(x,y)$ as

$$F(u,v) = \int_{-\infty}^{\infty}\int_{-\infty}^{\infty} \mu(x,y) e^{-i2\pi(xu+yv)} dxdy \tag{2.8}$$

Working in the rotate coordinate system $(t,s)$, the line integration in equation (2.7) is then simply the integration of the function $\mu'(t,s)$ along the $s$-axis

$$p_\theta(t) = \int_{-\infty}^{\infty} \mu'(t,s) ds \tag{2.9}$$

Denote the Fourier transform of $p_\theta(t)$ over variable $t$ as $P(\omega,\theta)$, as expressed by

$$\begin{aligned} P(\omega,\theta) &= \int_{-\infty}^{\infty} p_\theta(t) e^{-i2\pi\omega t} dt \\ &= \int_{-\infty}^{\infty}\int_{-\infty}^{\infty} \mu'(t,s) ds e^{-i2\pi\omega t} dt \\ &= \int_{-\infty}^{\infty}\int_{-\infty}^{\infty} \mu(x,y) e^{-i2\pi\omega t} ds dt \end{aligned} \tag{2.10}$$

From general theory of geometry, the two coordinate systems are related by the

following sets of equations

$$\begin{aligned} t &= x\cos\theta + y\sin\theta \\ s &= -x\sin\theta + y\cos\theta \end{aligned} \tag{2.11}$$

Then we have

$$\begin{aligned} dt\ ds = J\ dx\ dy &= \begin{vmatrix} \frac{\partial t}{\partial x} & \frac{\partial s}{\partial x} \\ \frac{\partial t}{\partial y} & \frac{\partial s}{\partial y} \end{vmatrix} dx\,dy \\ &= \begin{vmatrix} \cos\theta & -\sin\theta \\ \sin\theta & \cos\theta \end{vmatrix} dx\,dy \\ &= dx\,dy \end{aligned} \tag{2.12}$$

where $J$ is the Jacobian determinant. Combining equation (2.10), (2.11) and (2.12), we have

$$P(\omega,\theta) = \int_{-\infty}^{\infty}\int_{-\infty}^{\infty} \mu(x,y) e^{-i2\pi\omega(x\cos\theta + y\sin\theta)} dxdy \tag{2.13}$$

From equation (2.8) and (2.13), we find that if we let $u=\omega\cos\theta$ and $v=\omega\sin\theta$, the two equation become the same, which means

$$F(\omega\cos\theta, \omega\sin\theta) = P(\omega,\theta) \tag{2.14}$$

Also, the two variables $u=\omega\cos\theta$ and $v=\omega\sin\theta$ define a straight line through the origin whose angle with respect to $u$ axis is θ, as shown in Figure 2.7. Therefore, to perform the Fourier slice theorem, we perform the one dimensional Fourier transform on each projection and put it onto the corresponding position in two dimensional Fourier space. Once the entire Fourier transform is obtained, a simple 2D inverse Fourier transform

yields the reconstructed image.

### 2.3.3 Filtered backprojection (FBP)

Although the mathematical proof of Fourier slice theorem is straightforward, it presents significant challenges in actual implementation. The Fourier space defined by equation (2.14) is non-Cartesian. Since the Fourier slice theorem states that the 1D Fourier transform of a projection is a line through the origin in the 2D Fourier space, samples of all projection data eventually fall on a polar coordinate grid. Additionally, as the sensors are placed linearly, the samples from different projections will form concentric circles, as shown by the black points in Figure 2.8. Gridding or interpolation is necessary to produce a Cartesian grid (as depicted by the red grids in Figure 2.8) in order to take the inverse Fourier transform. However, gridding or interpolation in Fourier space is not straightforward because gridding errors in Fourier space are not localized in the spatial domain. Hence, any error on a single point in Fourier space can affect the whole appearance of the image.

Filtered backprojection (FBP) is a reformulation of the Fourier slice theorem. It is still one of the standard methods in clinical CT scanners. It avoids gridding and two dimensional Fourier transforms. In this section, we derive FBP for parallel beam geometry.

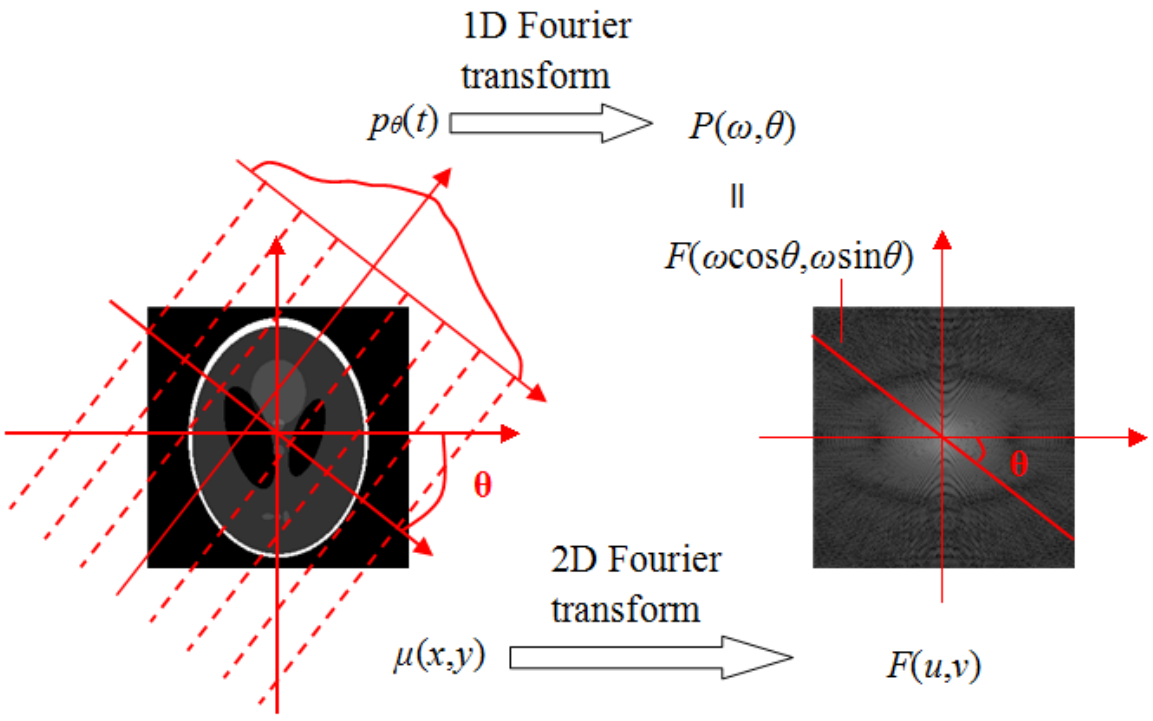


Figure 2.7 Illustration of Fourier slice theorem.

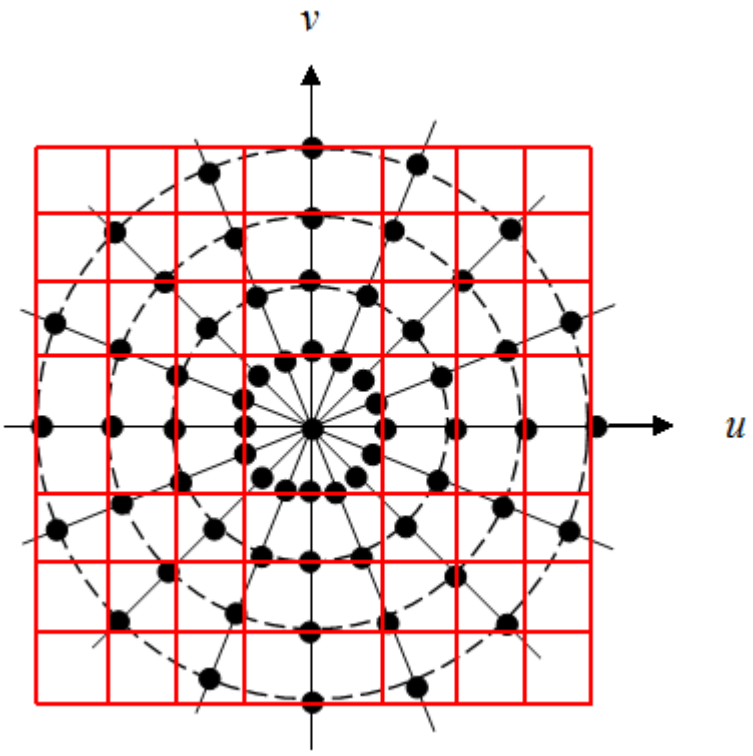


Figure 2.8 Sampling pattern in Fourier space by Fourier slice theorem.

From general signal processing theory, the image function, $\mu(x,y)$, can be obtained by performing the inverse Fourier transform on $F(u,v)$

$$\mu(x,y) = \int_{-\infty}^{\infty}\int_{-\infty}^{\infty} F(u,v)e^{i2\pi(xu+yv)}dudv \tag{2.15}$$

Recall from last section, we have

$$\begin{aligned} u &= \omega\cos\theta \\ v &= \omega\sin\theta \end{aligned} \tag{2.16}$$

then

$$\begin{aligned} du\,dv = J\,d\omega\,d\theta &= \begin{vmatrix} \dfrac{\partial u}{\partial \omega} & \dfrac{\partial v}{\partial \omega} \\ \dfrac{\partial u}{\partial \theta} & \dfrac{\partial v}{\partial \theta} \end{vmatrix} d\omega\,d\theta \\ &= \begin{vmatrix} \cos\theta & \sin\theta \\ \omega(-\sin\theta) & \omega\cos\theta \end{vmatrix} d\omega\,d\theta \\ &= \omega\,d\omega\,d\theta \end{aligned} \tag{2.17}$$

Combining equation (2.14), (2.15), (2.16) and (2.17), we obtain

$$\begin{aligned} \mu(x,y) &= \int_0^{2\pi} d\theta \int_0^{\infty} F(\omega\cos\theta,\omega\sin\theta)e^{i2\pi\omega(x\cos\theta+y\sin\theta)}\omega\,d\omega \\ &= \int_0^{2\pi} d\theta \int_0^{\infty} P(\omega,\theta)e^{i2\pi\omega(x\cos\theta+y\sin\theta)}\omega\,d\omega \\ &= \int_0^{\pi} d\theta \int_0^{\infty} P(\omega,\theta)e^{i2\pi\omega(x\cos\theta+y\sin\theta)}\omega\,d\omega \\ &+ \int_0^{\pi} d\theta \int_0^{\infty} P(\omega,\theta+\pi)e^{-i2\pi\omega(x\cos\theta+y\sin\theta)}\omega\,d\omega \end{aligned} \tag{2.18}$$

Taking the advantage of the symmetry properties of parallel beam geometry, $p_{\theta+\pi}(t)=p_{\theta}(-t)$, we have $P(\omega,\theta+\pi)= P(-\omega,\theta)$. Substituting this into equation (2.18), we can rewrite (2.18) as

$$\mu(x,y) = \int_0^{\pi} d\theta \int_{-\infty}^{\infty} P(\omega,\theta)|\omega| e^{i2\pi\omega(x\cos\theta + y\sin\theta)}\, d\omega$$
$$= \int_0^{\pi} d\theta \int_{-\infty}^{\infty} P(\omega,\theta)|\omega| e^{i2\pi\omega t}\, d\omega \qquad (2.19)$$

The inner integral in (2.19) is the inverse Fourier transform of P($\omega$,θ)|$\omega$|. In spatial domain, it means a projection is filtered by a function which has frequency respond as |$\omega$|. But in reality, this type of filter doest not exist as the magnitude can't increase to infinite. In discrete implementation, the filter, |$\omega$|, is implemented by the "Ram-Lak" filter or the "ramp" filter, which has a cutoff frequency at the Nyquist frequency, as shown in Figure 2.9. From the figure, we can see that the ramp filter tends to amplify high frequency noise. Also, from the knowledge of signal processing, the discontinuity in frequency domain cause pseudo gibbs phenomenon in image space. Therefore, design of effective filters that keeping small features of image while removing noise is still a challenge. The most important property of FBP is its fast speed. For this reason, the FBP or its variants, e.g., the Feldkamp-Davis-Kress (FDK) algorithm for cone beam, are used as a standard.

We denote the filter function as $f(t)$. Since P($\omega$,θ) is the Fourier transform of $p_\theta(t)$, we know from signal processing theory, the inverse Fourier transform of P($\omega$,θ)|$\omega$| equals the convolution between $p_\theta(t)$ and $f(t)$

$$g(t) = \int_{-\infty}^{\infty} P(\omega,\theta)|\omega| e^{i2\pi\omega t}\, d\omega$$
$$= p_\theta(t) \otimes f(t) \qquad (2.20)$$

where $\otimes$ represents the convolution operator. Equation (2.19) can be rewritten in the form

$$\mu(x,y)=\int_0^{\pi} g(t)d\theta \tag{2.21}$$

Equation (2.21) is a backprojection as it states that the reconstruction of a point ($x$,$y$) is the summation of all filtered projection samples that pass through that point. This can be done by backprojecting the filtered projections. Therefore, in order to reconstruct an image from parallel projections, we operate in the following steps:

1. Take one dimensional Fourier transform of each projection.
2. Multiply the Fourier transform P($\omega$,θ) by a function $|\omega|$.
3. Take the inverse Fourier transform of the filtered projections.
4. Backproject the filtered projections.

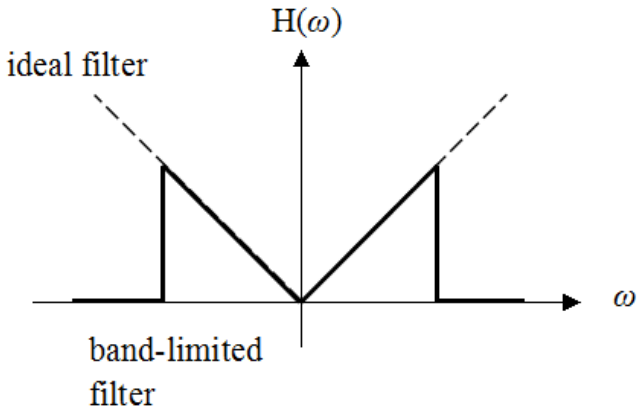


Figure 2.9 Frequency representation of the Ram-Lak filter

## 2.4 Iterative reconstruction technique

Iterative reconstruction techniques provide an entirely different approach for image reconstruction. In iterative reconstruction technique, the image reconstruction problem is

viewed as a system of linear equations. The unknown object image is found by solving the system iteratively. Let us order the two dimensional image in a one dimensional vector $\boldsymbol{\mu}=(\mu_1, \mu_2, ..., \mu_i, ..., \mu_n)$. And consider the measurements $\boldsymbol{p}=(p_1, p_2,..., p_j, ..., p_m)$ with $m$ the total number of projection values, i.e., the number of detectors multiplied by the number of angles. The imaging system is modeled by

$$p_j = \sum_{i=1}^{n} a_{ji}\mu_i + e_j \tag{2.22}$$

where $a_{ji}$ is the element of a system matrix, representing the contribution of pixel $i$ to the $j$th ray sum $p_j$, and $e_j$ represents the error caused by noise and measurement bias. Figure 2.10 shows an example of parallel beam CT system. Denote the system of linear equations as vector, we obtain

$$\mathbf{p} = \mathbf{A}\boldsymbol{\mu} + \mathbf{e} \tag{2.23}$$

where the system matrix **A** is determined by the CT geometry, focal spot and other physical parameters.

For a typical CT image, the system matrix is huge. For example, the system matrix will be in the order of $10^{12}$ for a $1000 \times 1000$ pixel image. Therefore, it is so difficult to solve the problem directly through matrix inversion. Alternatively, iterative reconstruction technique solve the problem iteratively and produce a sequence of solutions, $\boldsymbol{\mu}^{(0)}$, $\boldsymbol{\mu}^{(1)}$, $\boldsymbol{\mu}^{(2)}$, ..., $\boldsymbol{\mu}^{(k)}$, such that the sequence converges to $\boldsymbol{\mu}^{*}$, where $\boldsymbol{\mu}^{*}$ is the optimal solution based on the measurement data **p**. In each iteration, we perform a "forward projection" of the estimated image $\boldsymbol{\mu}^{(k)}$ to obtain a calculated projection. The

difference between the calculated projection $\mathbf{p}^{(k)}$ ($\mathbf{A}\boldsymbol{\mu}^{(k)}$) and the measured projection $\mathbf{p}$ is detected

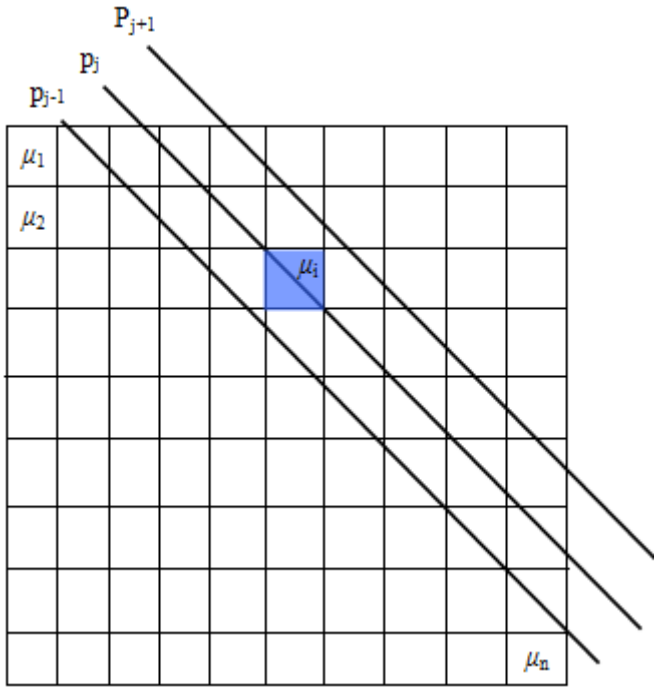


Figure 2.10 Illustration of iterative reconstruction technique. The blue area denotes the pixel $\mu_i$ contributes to the projection value $p_j$.

$$\mathbf{p} - \mathbf{p}^{(k)} \tag{2.24}$$

Based on the difference, we modify the next estimation $\boldsymbol{\mu}^{(k+1)}$ so that the difference will be reduced. The first iterative algorithm was proposed by Kaczmarz [6], namely algebraic reconstruction technique (ART). In each iteration, the difference is calculated for each view angle and backprojected to the estimation. ART iteration can be expressed by

$$\mu_i^{(k,j)} = \mu_i^{(k,j-1)} + \lambda_k \frac{p_j - \sum_i a_{ji}\mu_i^{(k,j-1)}}{\sum_i a_{ji}} a_{ji} \tag{2.25}$$

where $p_j$ is the $j$th component of the vector $\mathbf{p}$, $\lambda_k$ is a relaxation parameter and $j$=1,2,...,$m$.

Kaczmarz also define

$$\begin{aligned} \boldsymbol{\mu}^{(k,0)} &= \boldsymbol{\mu}^{(k-1)} \\ \boldsymbol{\mu}^{(k)} &= \boldsymbol{\mu}^{(k,m)} \end{aligned} \tag{2.26}$$

ART reconstruction is slow since it takes $m$ time of projection operator from $\boldsymbol{\mu}^{(k-1)}$ to $\boldsymbol{\mu}^{(k-1)}$ (see equation (2.25)). For a $1000 \times 1000$ pixel image and 1000 view angles, $m$ is in the order of $10^6$. Alternatively, simultaneous algebraic reconstruction technique (SART) was also proposed to recover the image iteratively. Different from ART, in which only one equation is used one time, SART involves all the equations at the same time in one iteration. SART computes an image update using the following recurrence equation[37]

$$\mu_i^{(k)} = \mu_i^{(k-1)} + \frac{\sum_j [a_{ji}(p_j - \sum_i a_{ji}\mu_i^{(k-1,j-1)})/\sum_i a_{ji}]}{\sum_j a_{ji}} \tag{2.27}$$

Compared to analytical reconstruction methods, iterative techniques have advantage of dealing with incomplete data set, such as the few view problem. ART and SART have proven to be able to get a better result than FBP. However, FBP strongly outperform ART and SART when it comes to hardware requirement and computation time. Figure 2.11 provides a straightforward example. The real image shown in Figure 2.11(a) is reconstructed from 360 views of projection data while (b) to (d) are reconstructed from 30 views of projections. The number of iterations of ART and SART are 40 and 150,

respectively. The reconstructions from ART and SART are better than FBP in terms of artifacts. But FBP is about 16 times faster than SART and 1100 times faster than ART. Additionally, the memory required by ART and SART is about 47 times of FBP.

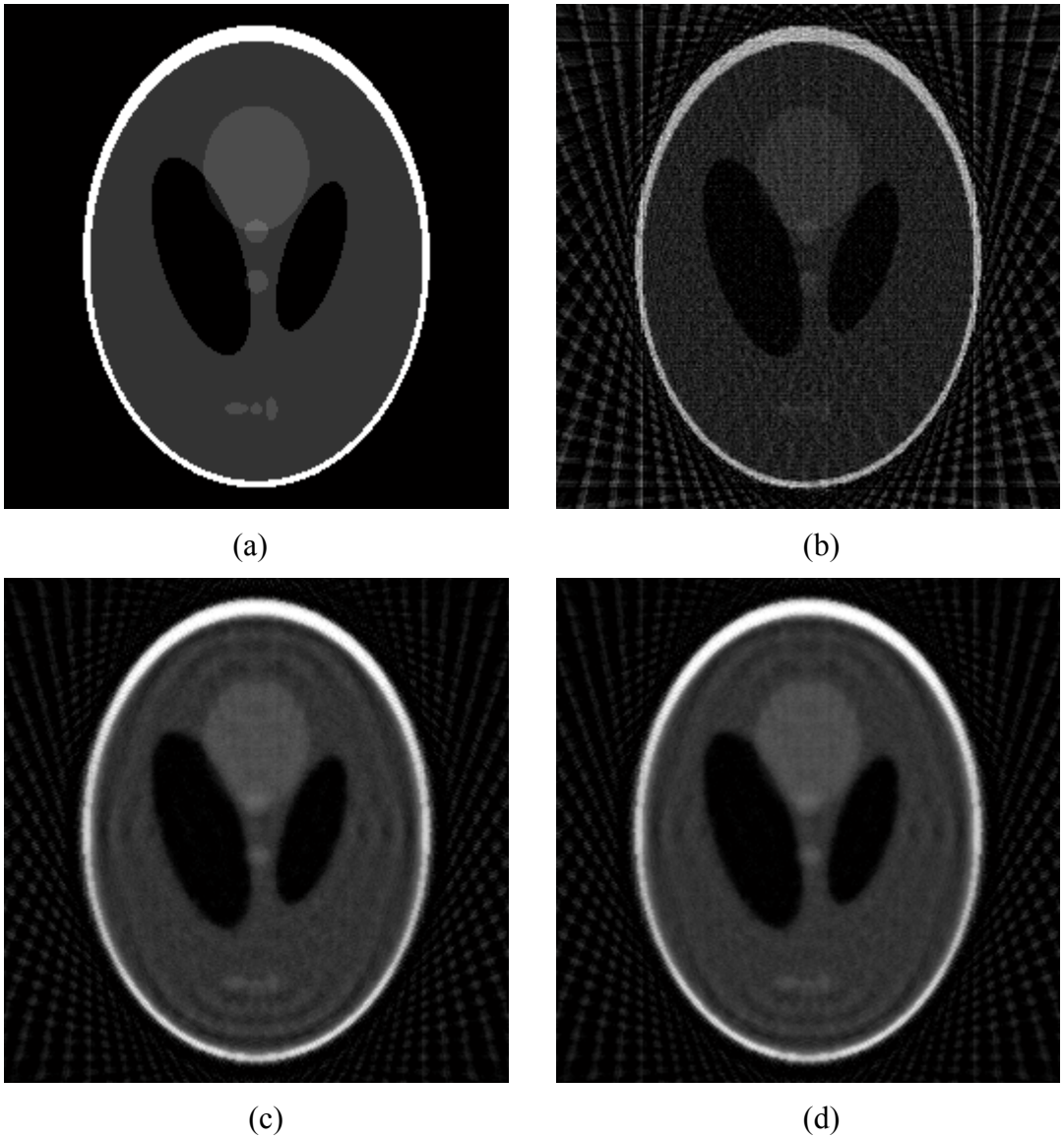

(a) (b)

(c) (d)

Figure 2.11 Reconstruction comparison between FBP and ART-type technique. (a) The real image; (b) FBP reconstruction; (c) ART reconstruction; (d) SART reconstruction.

## 2.5 Artifacts

An artifact can be any difference between the true attenuation coefficients of the object and the reconstructed image. One common artifact in CT images is streak artifact, as shown in Figure 2.11(b). They often occur around material with high attenuation. Many factors could contribute to streak artifact, such as beam hardening, photo starvation, undersampling etc. The following section discusses some of them.

**Beam Hardening**

Beam hardening is caused by the use of a polychromatic x-ray beam instead of monochromatic x-ray beam. As the beam passes through an object, the lower energy photons are absorbed more rapidly than higher energy photons. As a result, the mean energy of the beam increases. When the beam reaches the detector, the intensities are much higher than expected. This physical phenomenon causes two types of artifacts, cupping artifacts, streaks and dark bands.

**Partial Volume**

Partial volume occurs when X-ray CT can not distinguish between a large amount of low attenuation area and small amount of high attenuation area. This results in shading artifacts, but can be easily removed by using a thin acquisition width.

**Photon Starvation**

Photon starvation occurs when the x-ray is travelling through a highly attenuating areas, such as bones that absorbs most of the photons. As a result, few photons reach the

detectors, producing very noisy projections. When we reconstruct the image, the noise will be magnified, resulting in streaks in the image. A straightforward solution is to increase the power of x-ray beam. But the less attenuating parts of patient will receive an unnecessary dose. In addition, as discussed in Chapter 1, high radiation dose may potentially lead to a future increase risk of cancer.

**Undersampling**

As discussed in Chapter 1, fewer projection is one of development directions of CT. However, according to standard signal processing, if too few projections are taken, aliasing and fine stripes will present in the reconstructed image, making difficult to see edges and small objects. Figure 2.11(b) illustrates a combination of undersampling artifacts and streaking artifacts.

**Patient Artifacts**

There are two major types of patient based artifacts: metallic implant to such as total hip joint replacement and patient motion. Severe streaking artifacts occur when scanning very dense objects. Another type of patient artifacts is caused by patient motion during the scan. For more detailed discussion of CT artifacts, please refer to [38, 39].

Figure 2.12 is an example of streaking artifact. It was reconstructed from 50 views. Due to undersampling, streaking artifacts are presented in the image. The artifacts might be mistaken for disease in anatomy, compromising the image quality.

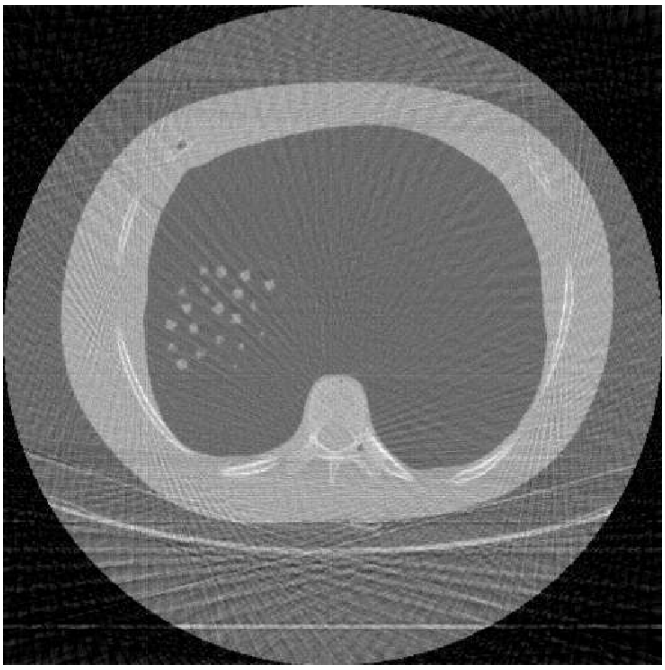

Figure 2.12 CT image shows streaking artifacts due to undersampling.

# Chapter 3

# Compressed Sensing and CT

## 3.1 Introduction

Compressed sensing (CS) [15-18] is an developing theory about signal acquisition and reconstruction. In traditional signal acquisition protocol, signal is sampled at the classical Shannon-Nyquist rate, in order to capture the entire information of the signal. In data compression stage, all the measurements are used to reconstruct the signal and a compression algorithm is applied to the reconstructed signal for further storage or transmission. At the beginning, CS emerges when people ask the question: Is it possible to build the data compression into the acquisition.

The major difference between CS and traditional signal processing method is its combination of data acquisition and data compression. In other words, CS only samples (approximately) as much as would be stored. By using CS, one can accurately recover a signal or an image from much fewer measurements than those obeying the Nyquist criterion. This framework is particularly useful in situations where a thorough acquisition of signal is expensive (MRI) or unsafe (CT). One crucial assumption in CS framework: the signal or image to be acquired must be sparse or compressible in a domain that it can be encoded with just a few coefficients without much loss of information. Fortunately,

this observation has been well studied in the area of image compression. An intuitive example of image compression is given in Figure 3.1, where three CT images are reconstructed using only the most significant 5% of the wavelet coefficients. The reconstructed images and the original images have no perceptual difference.

The data acquisition can be modeled by a system of linear equations

$$\mathbf{y} = \mathbf{A}\mathbf{x} \tag{3.1}$$

where $\boldsymbol{y}$ is the measurement vector in $\mathbf{R}^m$, $\boldsymbol{x} \in \mathbf{R}^n$ is the signal we want to reconstruct and $\mathbf{A}$ describes the acquisition model. In CS, data is acquired at much lower sampling rate than Nyquist rate, i.e., $m \ll n$. Equation (3.1) defines a vastly underdetermined system of equations. The simplest way to estimate $\mathbf{x}$ is through the least square method, minimizing the $\ell_2$-norm. The least square method is simple in mathematics, involving only matrix multiplication and pseudo-inversion. However, this method generally produces poor results for most applications. In the following sections, detailed discussion about CS will be given.

## 3.2 Framework of CS

Suppose the unknown vector $\boldsymbol{x}$ is compressible by transform coding using a known transform (e.g., Fourier or wavelet). Transform coding can be expressed by

$$\boldsymbol{\alpha} = \boldsymbol{\Phi}\mathbf{x} \tag{3.2}$$

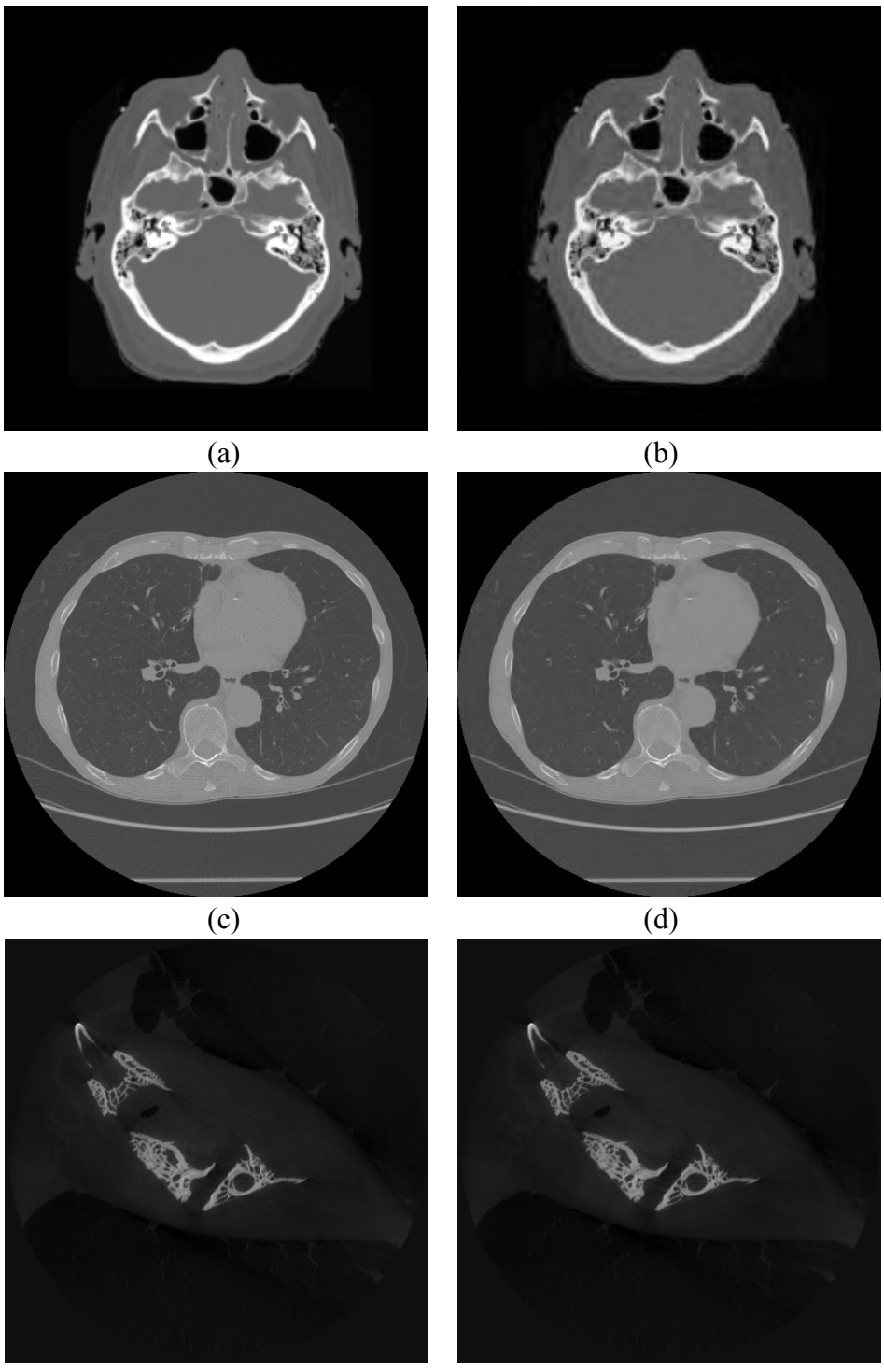

Figure 3.1 Illustration of CT image compression using wavelet transform. From top to bottom are base of skull, chest and fish jaw CT images, respectively. Left side are original images and right side are reconstructed images from the most significant 5% of wavelet coefficients.

where $\boldsymbol{\alpha}$ is the transform coefficient vector of $\boldsymbol{x}$ in the domain $\boldsymbol{\Phi}$. By assuming $\boldsymbol{x}$ is compressible by transform coding, we mean that $\boldsymbol{\alpha}$ has only $k$ elements with relatively large magnitudes. Reconstruction error with these $k$ most important coefficients will be bounded by a small value ε

$$\left\|\mathbf{x}-\mathbf{x}_k\right\|_2=\left\|\boldsymbol{\alpha}-\boldsymbol{\alpha}_k\right\|_2<\varepsilon \tag{3.3}$$

where $\boldsymbol{\alpha}_k$ is obtained by keeping the $k$ most important coefficients in $\boldsymbol{\alpha}$ and setting zeros elsewhere, $\mathbf{x}_k$ is the reconstruction from $\boldsymbol{\alpha}_k$.

CS consists of three stages [40]: encoding, sensing and decoding. In the first stage, the object image $\boldsymbol{x}$ is encoded into a smaller vector $\mathbf{y} = \mathbf{A}\boldsymbol{x}$ by the system matrix, as shown in Section 3.1. Then the second stage is acquiring the undersampled measurements $\mathbf{y}$ from the imaging system. In the third stage, CS incorporates the prior knowledge into the process of image reconstruction. Theoretically, CS reconstructs the signal or image by minimizing the $\ell_0$-norm as

$$\min_{\mathbf{x}}\left\|\boldsymbol{\Phi}\mathbf{x}\right\|_0 \quad \textit{subject to} \quad \mathbf{A}\mathbf{x}=\mathbf{y} \tag{3.4}$$

where the $\ell_0$-norm $\|\cdot\|_0$ is the nonzero components of a vector. Equation (3.4) will find a signal that has the sparsest representation in $\boldsymbol{\Phi}$ while still gives the output $\boldsymbol{y}$ when it is the input to the system. There are two things making it impractical to solve (3.4) directly. First, most natural signals or images are compressible rather than sparse. The more important is that solving the $\ell_0$-norm minimization problem requires combinatorial

optimization[41]. Donoho[42] proved that the solution to $\ell_1$-norm minimization is a good approximation to $\ell_0$-norm minimization problem. The advantage of $\ell_1$-norm minimization is that it is more computationally tractable and can be solved by some existing linear programs[43, 44]. The equivalent $\ell_1$-norm problem of (3.4) is expressed by

$$\min_{\mathbf{x}} \|\mathbf{\Phi x}\|_1 \quad subject\ to\ \ \mathbf{Ax} = \mathbf{y} \tag{3.5}$$

where the $\ell_1$-norm $\|\cdot\|_1$ is the sum of absolute value of a vector. Mathematical speaking, it is possible to reconstruct $\boldsymbol{x}$ from $m = O(k\ln(n))$ measurements by solving (3.5). But in most practical situations, acquired data is imperfect, i.e., measurements are disturbed by noise: $\boldsymbol{y}$=$\mathbf{A}\boldsymbol{x}$+$\mathbf{e}$. It is assumed that the perturbation is bounded by a known amount $\|\mathbf{e}\|_2 < \sigma$. This gives rise to

$$\min_{\mathbf{x}} \|\mathbf{\Phi x}\|_1 \quad subject\ to\ \|\mathbf{Ax} - \mathbf{y}\|_2 < \sigma \tag{3.6}$$

where σ is a parameter controlling the data consistency. By Lagrange theorem, the constrained problem in (3.6) can be further translated into an unconstrained problem

$$\min_{\mathbf{x}} \lambda\|\mathbf{\Phi x}\|_1 + \|\mathbf{Ax} - \mathbf{y}\|_2^2 \tag{3.7}$$

In the last few years, a huge variety of algorithms for solving the optimization problem (3.6) have been proposed and studied. Some of these methods include: interior point methods [45, 46], projected gradient methods [47, 48], iterative thresholding[49], iteratively reweighted least squares[50], and matching pursuit. The interior point methods are guaranteed to get a precise solution in time $O(m^2n^{1.5})$ [51]. For most practical problem,

the constant $m^2n^{1.5}$ is quite large. Therefore, interior point methods are considered slow. Projected gradient methods, on the other hand, are much faster than interior point methods while still maintaining good precision. A greedy iterative algorithm called orthogonal matching pursuit (OMP) and its variants were also proposed in literature. OMP was proved to work well with sparse and noise free signal. But it is still unknown whether it succeeds for compressible or noisy signals[41]. The accuracy of iterative thresholding methods highly depend on the initial guess. They are only guaranteed to find a local optimal solution. So far, it is impossible to say that which one is the best method to solve equation (3.7). All these methods have their advantages and disadvantages. In next chapter, we describe our approach to solve (3.7).

## 3.3 Compressed sensing in CT

Due to its powerful ability of reconstructing signal or image from highly undersampled data, CS has attracted tremendous attention in medical imaging community since it was introduced by Donoho et al. in 2006. The first attempt to apply CS to medical imaging was done by Lustig et al. in [52], in which they successfully reconstructed MR images with 40% of the data. Since then, large amount of papers were published on compressed sensing MRI. There are also research efforts on compressed sensing CT. Because in principle a CS based algorithm can produce good reconstructions using fewer

samples (projections), it has the potential to reduce the radiation exposure to the patient, a problem that has received much attention in recent years. Furthermore, as discussed in previous section, there are large amount of methods to solve the minimization problem, of which have a unique solution and can be solved efficiently (i.e. with fast convergence). Putting CS in the context of the body of CT imaging, we have

$$\min_{\boldsymbol{\mu}} \lambda\left\|\boldsymbol{\Phi}\boldsymbol{\mu}\right\|_1 \quad subject\ \ to \quad \left\|\mathbf{A}\boldsymbol{\mu}-\mathbf{p}\right\|_2^2 < \sigma \tag{3.8}$$

The most popular type of method that has been studied is the Total Variation (TV) based compressed sensing methods [22-24, 53-55]. Although there are lots of variants of TV based methods, the performance of these methods are quite similar. TV based methods use total variation as a sparsity transform. In general, TV based methods can be expressed by

$$\boldsymbol{\mu} = \arg\min_{\boldsymbol{\mu}} J(\boldsymbol{\mu}) = \arg\min_{\boldsymbol{\mu}} \lambda\left\|\boldsymbol{\mu}\right\|_{TV} + \left\|\mathbf{A}\boldsymbol{\mu}-\mathbf{p}\right\|_2^2 \tag{3.9}$$

where the regularization factor λ is introduced to leverage the cost function's emphasis on the sparseness prior and the data fidelity term. The selection of this regularization factor has been studied a lot in the area of regularized iterative methods [56-58]. A well known approach to find the best one is via the *L* curve. The TV term of an image in this work is defined as follows:

$$\left\|\boldsymbol{\mu}\right\|_{TV} = \int\left|\nabla\boldsymbol{\mu}\right|\mathrm{d}x \tag{3.10}$$

In a discrete version, equation (3.10) becomes

$$\|\boldsymbol{\mu}\|_{TV} = \sum_{i,j} \sqrt{(\nabla \boldsymbol{\mu}_x^2)_{i,j} + (\nabla \boldsymbol{\mu}_y^2)_{i,j}} \tag{3.11}$$

where $\nabla \boldsymbol{\mu}_x$ , $\nabla \boldsymbol{\mu}_y$ represent the finite differences of the image along *x* and *y* direction. In such approaches, since TV corresponds to image gradient, minimizing it will greatly remove high spatial gradient elements such as noise and streaking artifacts, resulting in better reconstruction than FBP and other iterative reconstruction methods. Such approaches can be easily applied to fan beam or cone beam CT.

Some research efforts have also been done to apply CS to dynamic CT imaging. PICCS [21, 59] is one of the best methods that have been reported. In dynamic CT imaging, a sequential scan of the same image slice is obtained in order to study the dynamical change in the image object. In the PICCS method, a prior image ($\boldsymbol{\mu}_p$) is reconstructed using the standard FBP algorithm from the full data set, which is densely sampled over the scanning angular range (1000-2000 views). With such many views of projection data, the prior image is considered to be accurate and is used to constrain the CS image reconstruction. And then PICCS subtracts the target image from the prior image $\boldsymbol{\mu}-\boldsymbol{\mu}_p$, which will cancel the static structures, sparsifying the target image. Finally, a general CS algorithm is used to reconstruct $\boldsymbol{\mu}-\boldsymbol{\mu}_p$ and thus $\boldsymbol{\mu}$. PICCS reconstructs image by solving the following problem:

$$\min_{\boldsymbol{\mu}} [\alpha \left\| \boldsymbol{\Phi}(\boldsymbol{\mu} - \boldsymbol{\mu}_p) \right\|_1 + (1-\alpha) \left\| \boldsymbol{\Phi}\boldsymbol{\mu} \right\|_1] \quad \textit{subject to} \quad \left\| \mathbf{A}\boldsymbol{\mu} - \mathbf{p} \right\|_2^2 < \sigma \tag{3.12}$$

In particular, in [21], TV is selected for $\boldsymbol{\Phi}$. One can compare equation (3.8) with (3.12) and find that, if α is set to be 0, PICCS method is essentially the extension of TV methods

on dynamic CT imaging. Table 3.1 summarize the reconstructions algorithms that will be compared in this thesis.

Since this thesis only considers 2D static CT imaging, TV methods are used to compare the performance of the proposed algorithm.

Table 3.1 Summary of CT reconstruction techniques

| | FBP | ART | SART | TV |
|---|---|---|---|---|
| Reconstruction time | low | medium | low | high |
| Accuracy | low | medium | medium | high |
| Computer hardware requirement | low | high | high | medium |
| Capability to handle incomplete data | low | medium | medium | high |
| Sensitivity to noise | high | medium | medium | low |
| Geometry free | no | yes | yes | yes |

# Chapter 4

# Improved compressed sensing algorithm for sparse-view CT

## 4.1 Context

The ingredients of CS theory as well as the integration within the CT imaging system have been discussed in Chapter 3. Additionally, the recently proposed TV based methods and PICCS have been reviewed. TV based methods have proven to be powerful in CT image reconstruction in literature. Despite the great success of the TV model in terms of reconstructing high-quality images, one serious disadvantage undermines its application. The major problem of TV based compressed sensing methods is that they try to uniformly penalize the image's gradient irrespective of the underlying image structures. As a result, edges with low contrast regions are sometimes over smoothed, causing loss of low-contrast information and fine details [14]. To resolve this issue, we propose a novel algorithm based on compressed sensing that jointly minimizes the wavelet transform and total variation of the object image. 2-D wavelet transforms are good at capturing point singularities [26], thus preserving fine structure and low contrast information. This process suppresses the streaking artifacts and noise, while detailed structures are also preserved, resulting in an improved image.

## 4.2 Problem reformulation

We propose a novel compressed sensing based method by combining two sparsity transforms: TV and wavelet. Wavelet is good at preserving small features and low contrast information while TV is efficient at suppressing noise and streaking artifacts. In this way, we obtain a good balance between streaking artifacts suppression and detail preservation. Our iterative reconstruction algorithm solves the image via the following optimization problem[60]:

$$\boldsymbol{\mu} = \arg\min_{\boldsymbol{\mu}} J(\boldsymbol{\mu}) = \arg\min_{\boldsymbol{\mu}} \lambda_1 \left\| \boldsymbol{\mu} \right\|_{TV} + \lambda_2 \left\| \boldsymbol{\Phi\mu} \right\|_1 + \left\| \mathbf{A\mu}\text{-}\mathbf{p} \right\|_2^2 \qquad (4.1)$$

where $\boldsymbol{\Phi}$ denotes the wavelet transform operator. The two regularization factors $\lambda_1$ and $\lambda_2$ control the amount of smoothing. A large $\lambda_1$ and small $\lambda_2$ is not able to capture enough detail information. In such a circumstance, the algorithm reduces to the TV method. In contrast, small $\lambda_1$ and large $\lambda_2$ tend to give low weights to image gradients, making the method inefficient at suppressing noise and streaking artifacts. The optimized selection of $\lambda 1$ and $\lambda 2$ is discussed in the following section. We exploit a fast implementation of the wavelet transform [61], which speeds up the implementation.

As discussed in Chapter 3, there are many existing methods to solve equation (4.1). In this thesis, we propose solving it using a nonlinear conjugate gradient descent algorithm with backtracking line search [62] where $J(\boldsymbol{\mu})$ is the cost function as defined in (4.1). Nonlinear conjugate gradient descent algorithm is previously studied that it has global convergence and the running time is low compared to interior point methods[63].

ITERATIVE ALGORITHM FOR $\ell_1$ MINIMIZATION

INPUTS:

$p$ - undersampled projection data

$A$ - system matrix associated with the measurements

$\Phi$ - wavelet transform operator

$\lambda_1, \lambda_2$ - tuning constants

OPTIONAL PARAMETERS:

Tol - stopping criteria by gradient magnitude (default $10^{-4}$)

Iter - stopping criteria by number of iterations (default 100)

$\alpha, \varsigma$ - line search parameters (defaults $\alpha = 0.01$, $\varsigma = 0.6$)

OUTPUTS:

$\mu$ - the numerical approximation to equation (17)

% Initialization

$k$=0; $\mu_0=\mu_{FBP}$; $g_o=\nabla J(\mu_0)$; $\Delta\mu_0=- g_o$

% Iterations

*while* ( $||g_k||_2 >$ Tol)

{

% Backtracking line-search

$t$=5; *while* ($J(\mu_k+t\Delta\mu_k) > J(\mu_k) +\alpha t \cdot Real(g_k^* \Delta\mu_k)$ and $k <$ Iter )

$\{t=\varsigma\, t\}$

$\mu_{k+1} = \mu_k + t\Delta\mu_k$

$g_{k+1} = \nabla J(\mu_{k+1})$

$\eta_k = \quad g_{k+1} - g_k$

$$\beta_{k+1} = \max\{0, \min\{\frac{g_{k+1}^T \eta_k}{\Delta\mu_k^T \eta_k}, \frac{\left\|g_{k+1}\right\|^2}{\Delta\mu_k^T \eta_k}\}\}$$

$\Delta\mu_{k+1} = - g_{k+1} + \beta_{k+1}\Delta\mu_k$

$k = k+1$ }

---

The conjugate gradient requires the computation of $\nabla J(\mu)$ which is,

$$\nabla J(\boldsymbol{\mu}) = \lambda_1 \nabla \left\|\boldsymbol{\mu}\right\|_{TV} + \lambda_2 \nabla \left\|\boldsymbol{\Phi\mu}\right\|_1 + 2\mathbf{A}^*(\mathbf{A\mu} - \mathbf{p}) \qquad (4.2)$$

As the $\ell_1$ norm and total variation term (equation (3.10)) is the sum of absolute values. The absolute value, however, is not a smooth function and as a result equation (4.2) is not well defined. In [52], Lustig et al. approximated the absolute value with a smooth function $|x| \approx \sqrt{x^* x + \xi}$ , where $\xi$ is a positive smoothing parameter. Then the gradient becomes, $d|x| \approx \frac{x}{\sqrt{x^* x + \xi}}$.

We adopt this idea in our implementation. In particular, a smoothing factor $\xi = 10^{-15}$ is used. The flow chart of the implementation is given in Figure 4.1.

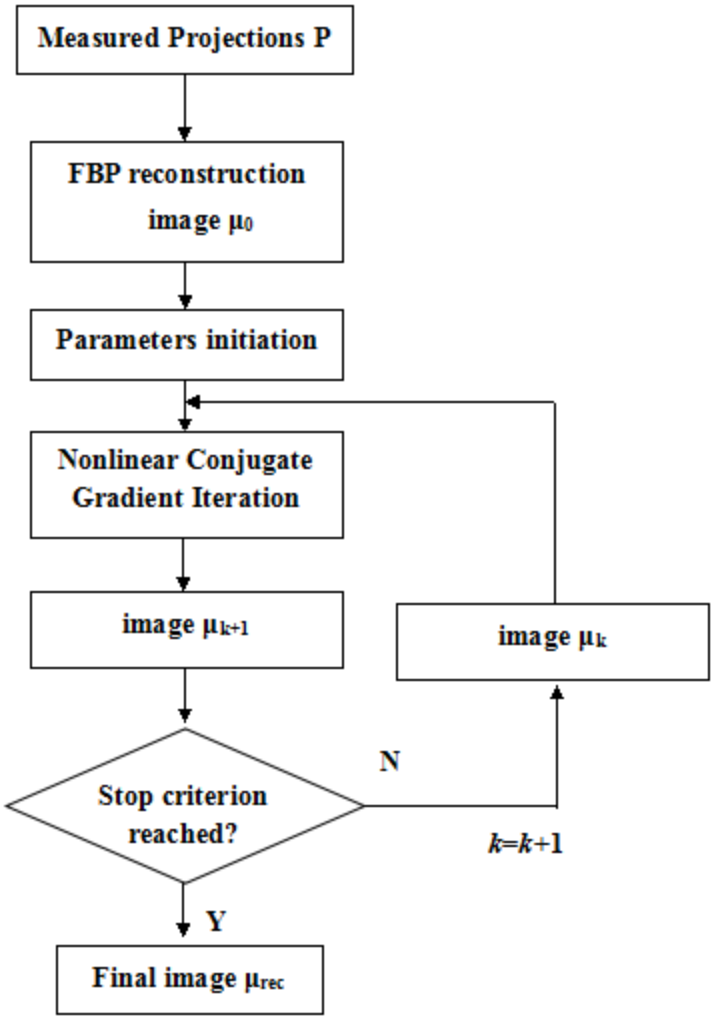


Figure 4.1 Flow chart of the implementation of the proposed algorithm.

## 4.3 Image quality assessment

To quantitatively study the accuracy of the algorithm, we use three metrics to measure the similarity between the ground truth image and the reconstructed images. The first metric is the relative error metric, which was calculated for the images reconstructed from each methods under different conditions for comparison. The relative root mean

square error (*RRMSE*) is defined as:

$$RRMSE = \frac{\left\| \mu - \mu_{ref} \right\|_2}{\left\| \mu_{ref} \right\|_2} \tag{4.3}$$

where $\mu$ is the reconstruction image by the proposed method, and $\mu_{ref}$ is the reference image. Since undersampling streak artifacts are an important feature in sparse-view CT image reconstruction, streaking level is also quantified by the streak indicator (*SI*). *SI* is based on the TV values stemming from streak artifacts. First introduced in [64], it has been used as a metric to quantify streak artifacts in [53] and [65]. The streak indicator (*SI*) is defined as:

$$SI = TV(\mu - \mu_{ref}) \tag{4.4}$$

The lower the value of *SI*, the less streaking artifacts are present in the reconstructed image.

The structural similarity (SSIM) index is highly effective for measuring the structural similarity between two images. Suppose $\rho$ and $t$ are local image patches taken from the same location of two images that are being compared. The local SSIM index measures three similarity of the image patches: the similarity of luminances $l(\rho,t)$, the similarity of contrasts $c(\rho,t)$ and similarity of structures $s(\rho,t)$. Local SSIM is defined as

$$\begin{aligned} S(\rho,t) &= l(\rho,t) \cdot c(\rho,t) \cdot s(\rho,t) \\ &= \left(\frac{2\mu_\rho \mu_t + C_1}{\mu_\rho^2 + \mu_t^2 + C_1}\right)\left(\frac{2\sigma_\rho \sigma_t + C_2}{\sigma_\rho^2 + \sigma_t^2 + C_2}\right)\left(\frac{\sigma_{\rho t} + C_3}{\sigma_\rho \sigma_t + C_3}\right) \end{aligned}$$

where $\mu_\rho$ and $\mu_t$ are local means, $\sigma_\rho$ and $\sigma_t$ are local standard deviations and $\sigma_{\rho t}$ is cross

correlation after removing their means. $C_1$, $C_2$ and $C_3$ are stabilizers. The SSIM index is computed locally within a moving kernel for each pixel and eventually generating a SSIM map. The SSIM index of the entire image can be computed by any method using the SSIM map, e.g., simply averaging the SSIM map. Although in other papers, such as in [54], a metric name universal quality index (UQI) was used, SSIM is actually an improved version of the algorithm [66]. Also, the correlation coefficient (CC) defined in [54] is actually the similarity of structures $s(\rho,t)$ in SSIM. Hence, SSIM is highly effective for measuring image quality and employed in this thesis for fair comparison. The higher the value of *SSIM*, the higher image quality is delivered.

## 4.4 Material and Methods

There are five sets of experiments. In the first two experiments, actual CT images and simulated projections were used to study the performance of our algorithm under ideal and degraded conditions. The last three experiments used real data collected using the Canadian Light Source (http://www.lightsource.ca/) and University of Saskatchewan facilities. In all cases, we investigated reconstructions from 20, 30, 40, 50, 60, 70, 80, 90, 100, 110, up to 120-view datasets extracted from the full dataset, respectively, representing different levels of data sampling. The study showed how the varying degree of sampling impacts the reconstruction. In each case, a uniformly spaced view angle data

decimation reduced scheme over $180^0$ was used to obtain undersampled data. To have a comparison between existing algorithms, all datasets were also reconstructed with FBP, ART, SART and TV methods. We implemented ART with the original method presented in [6].

In order to find the optimum number of iteration, we have conducted another experiment using simulated phantom. The results are shown in Figure 4.2. It can be seen from Figure 4.2(a) that the RRMSE of ART becomes almost unchanged after 30 iterations. Hence, 30 is used as the optimum number of iterations for ART for all experiments. Similarly, the optimum number of iterations for SART, TV, and the proposed method is also estimated, and 150 is used for them. To verify the number of iterations, the experiments were repeated on noisy phantom and real data, and the results were found to be consistent with that of Figure 4.2.

Moreover, the reconstruction accuracy depends on the selection of optimum regularization parameters for both TV method and the proposed method. We have used a real dataset (such as rat dataset as described later) using 50 projections as an example to show the methodology of determining the optimal parameters. For TV method, the reconstruction error is plotted against $\lambda$ (equation (3.9)) as shown in Figure 4.3(a). The lowest reconstruction error is obtained when $\lambda$ is between 0.0005 and 0.001. In this study, we have selected $\lambda = 0.0005$. The optimal $\lambda$ for all datasets is shown in the following sections.

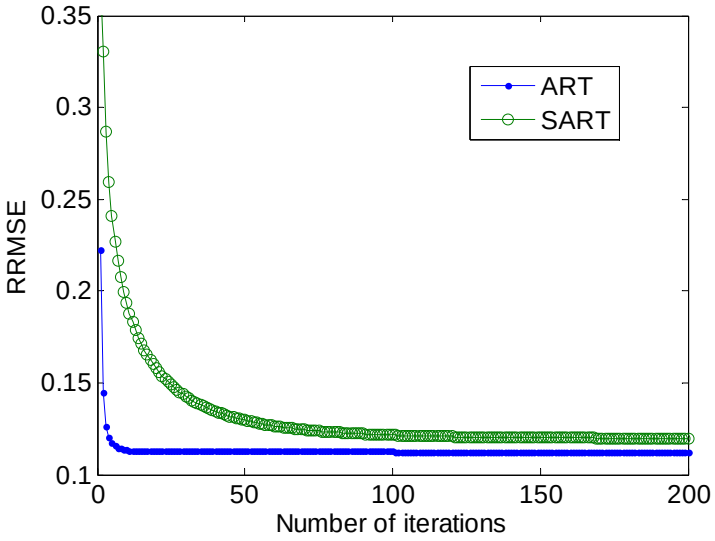


(a)

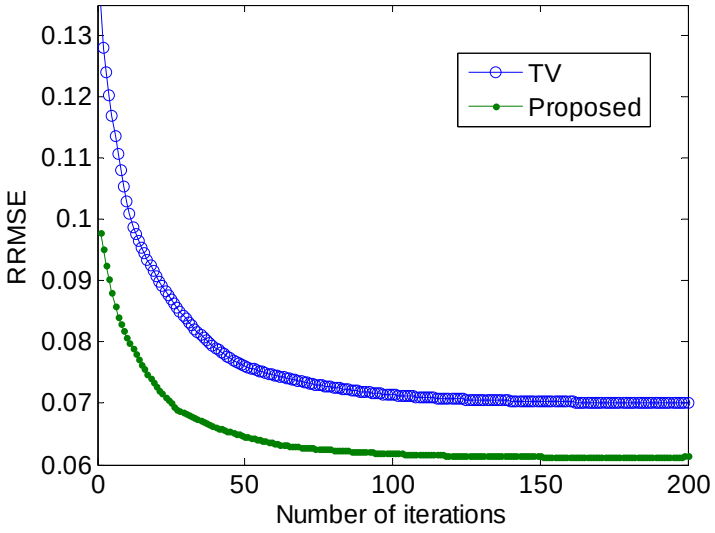


(b)

Figure 4.2 Analysis to find the optimum number of iterations for different methods: (a) ART and SART, (b) TV and the proposed scheme.

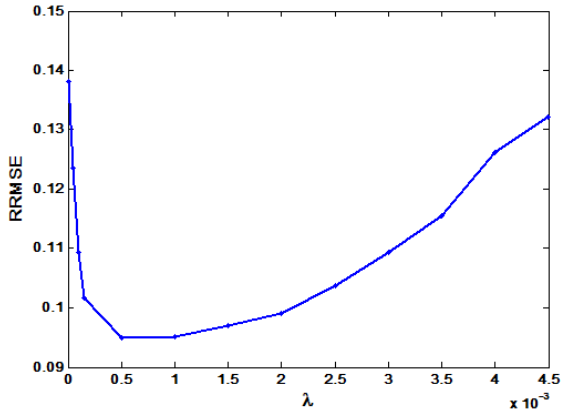


(a)

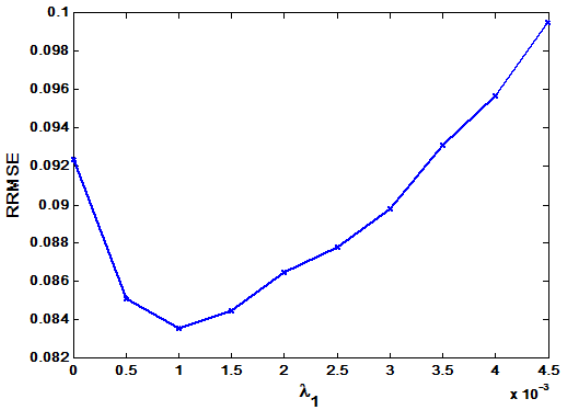


(b)

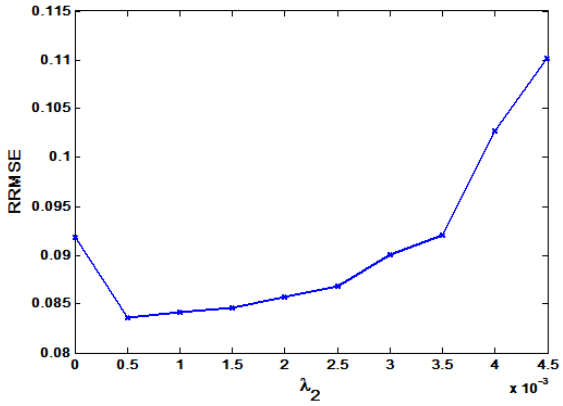


(c)

Figure 4.3: Analysis to find the optimum regularization parameters (for rat dataset): (a) $\lambda$ in TV method; (b) $\lambda_1$ when $\lambda_2 = 0.0005$ for the proposed method; (c) $\lambda_2$ when $\lambda_1 = 0.001$ for the proposed method.

For the proposed algorithm, there are two parameters. We alternately plotted the reconstruction error against one parameter keeping the other fixed. We started by setting $\lambda_2 = 0.0005$. Figure 4.3(b) shows that the lowest reconstruction error is obtained when $\lambda_1$ is 0.001. Then we set $\lambda_1$ to 0.001 and searched the optimal value for $\lambda_2$ that gives the lowest error, as shown in Figure 4.3(c).Thus, we used this recurring process to determine the optimum values of $\lambda_1$ and $\lambda_2$. Similar search was conducted for all dataset. The optimal values of these parameters are shown for each data set. The full-view FBP reconstruction image was used as the reference.

## 4.5 Simulation Results

In this section we present 2D reconstructions results using simulated data based on the reconstruction algorithm discussed in previous section. In order to demonstrate its effectiveness, we make a comparison on different simulated data. We simulated a parallel beam geometry, but the algorithm should apply equally well to other geometries.

**Phantom image** The phantom image used in this section is shown in Figure 4.4(a). It is a nodule phantom image provided free of charge by the National Cancer Institute (NCI) [67]. We used a central slice of the three dimensional data set as a sample set. We suppose that it is the desired CT image and each pixel value presents an attenuation coefficient.

The sample image was 512×512. This nodule phantom has objects with a variety of attenuation coefficients as well as small and low contrast structures.

**Real CT image** This real CT image was an axial scan of the skull base from a female cadaver by the N.I.H. in the United States [68]. It was taken with 0.33 cubic mm voxels, and cropped with a resolution of 360×360 pixels for better demonstration, as shown in Figure 4.4(b). The skull base is highly attenuating. According to the discussion of artifacts in Chapter 3, there will be steak artifacts in reconstructed images.

**Simulated projection data** Unless specified, the simulated projection data were obtained by computing the line integrals across the image with different views uniformly distributed over $180^o$.

### 4.5.1 Simulation without noise

In the first set of experiment, simulated projection data is generated by forward projection without any noise purposely added. The reconstructed images using 50 views are selected for demonstration. The optimal $\lambda$, $\lambda_1$ and $\lambda_2$ are summarized in Table 4.1.

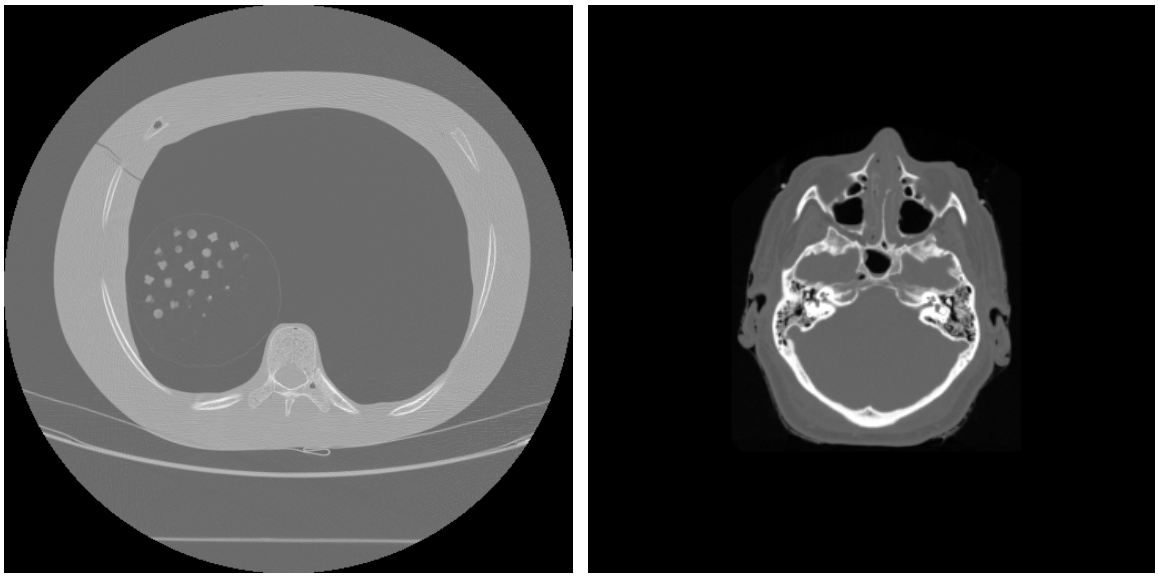

(a) (b)

Figure 4.4 Reference images for simulation experiments. (a) Nodule phantom image. (b) Head image. Gray level is normalized in [0, 1].

The reconstructions for Nodule phantom are shown in Figure 4.5. As can be noticed from Figure 4.5(b), the conventional FBP algorithm is not able to reconstruct diagnostically satisfactory image with such few projections and strong streaking artifacts are present in reconstructed image. Although streaking artifacts have been greatly reduced in ART and SART reconstructions, we can still see streaking artifacts in smooth regions, as indicated by black arrows in the figure. In contrast, even with such few views of data, both the TV method and proposed algorithm can still capture most of the structures, leading to visually improved results.

However, we can still see the residual streak artifacts in the TV reconstruction. The

image reconstructed from our proposed method shows the least level of streaking artifacts. One possible reason to explain that is, in wavelet domain, the noise is uniformly spread throughout the coefficients while most of the image information is concentrated in the few largest coefficients[69, 70]. Hence noise is potentially small values in wavelet domain. As equation (4.1) tries to minimize the ℓ1 norm of wavelet coefficients, small values corresponding to noise and artifacts are also suppressed, leading to better reconstruction. Besides, TV-base methods, including our algorithm tend to remove small structure and degrade the image resolution and image quality. But compared to TV method, our proposed method has slightly advantage in preserving edges information. To see it clearly, detailed expansions are shown in Figure 4.6.

Table 4.1: Optimum parameter selections for simulated experiment without noise

| Data | TV algorithm | Proposed algorithm | |
|---|---|---|---|
| | $\lambda$ | $\lambda_1$ | $\lambda_2$ |
| Nodule phantom | 0.0005 | 0.0005 | 0.0005 |
| Head | 0.0008 | 0.0005 | 0.0006 |

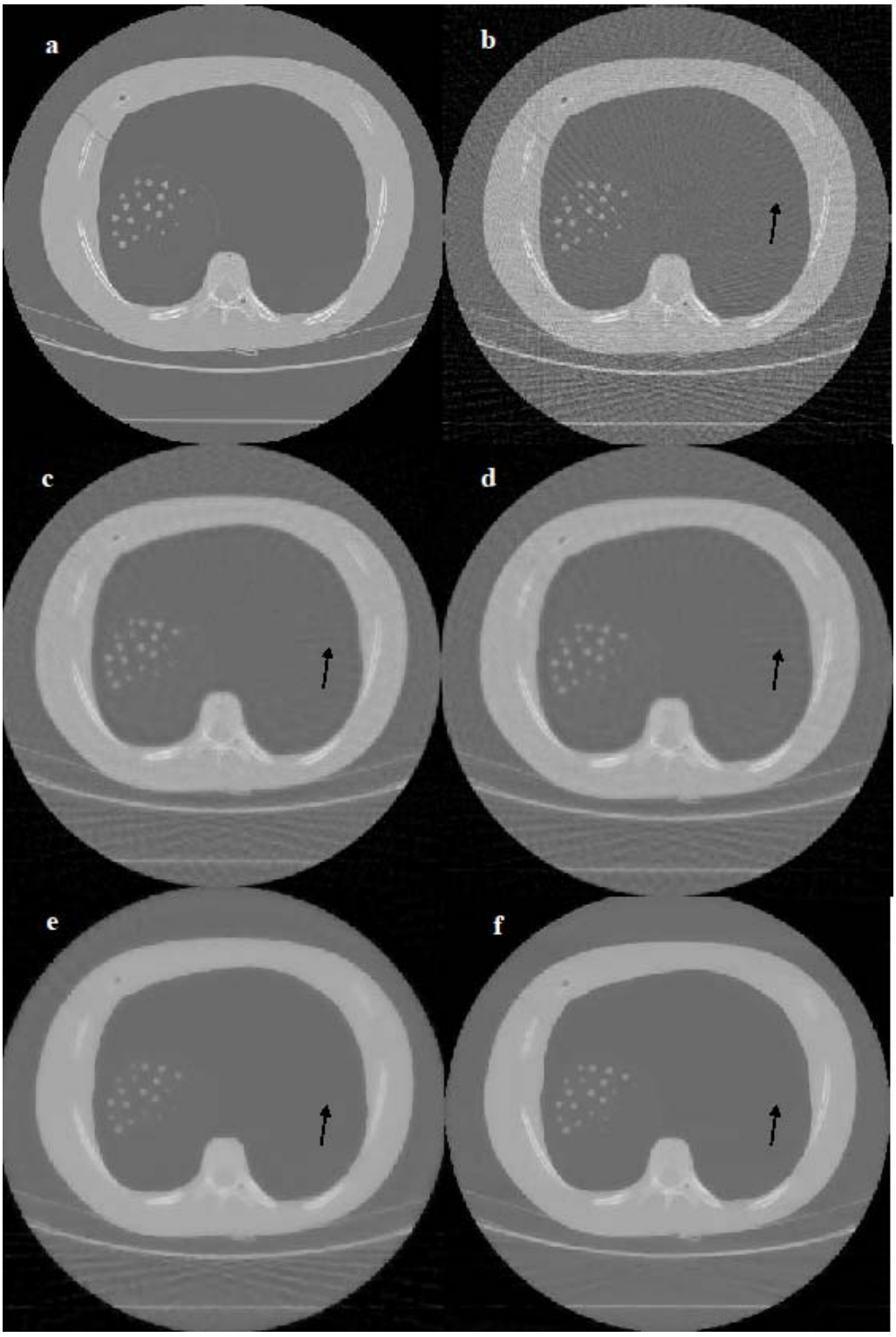


Figure 4.5 The reconstruction results of the nodule phantom using 50 views. (a) The ground truth image reconstructed with 1080 views, (b) the result obtained using FBP algorithm, (c) the ART algorithm, (d) the SART algorithm, (e) the TV algorithm, and (f) our proposed CS algorithm.

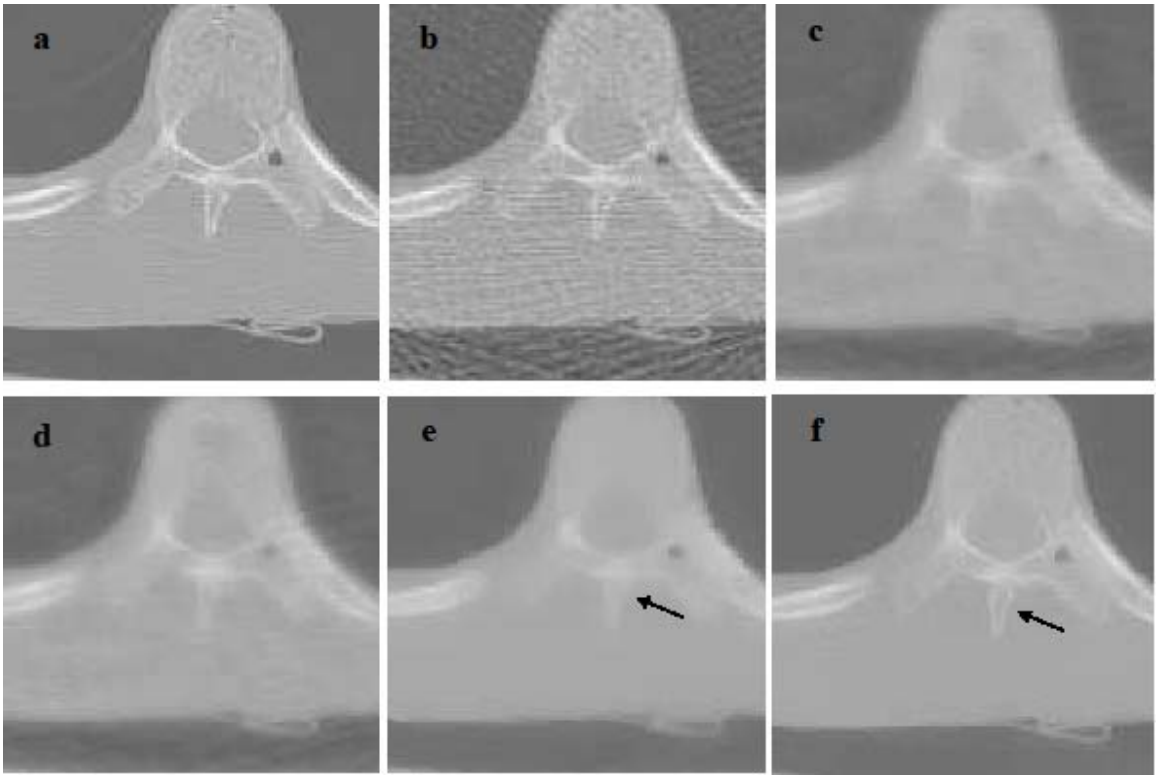


Figure 4.6 A detailed subsection of Figure 4.5: (a) ground truth, (b) FBP method, (c) ART method, (d) SART method, (e) TV method, and (f) the proposed method.

We can see from Figure 4.6, both TV method and the proposed method can further remove the streaking artifacts that are presented in ART and SART reconstructions. But the fine structures get blurred as TV suppress the gradient of the image. As indicated by the black arrows, the low contrast edges are better reconstructed by our proposed method. To quantify the results, we also show the RRSME, SI and SSIM value of the reconstructed images of Figure 4.5 in Table 4.2. Clearly, the result from our method has lower error level, less streak artifacts and higher structural similarity. With these results, we can see that our method is superior to the other methods.

Table 4.2 Reconstruction results with 50 views using phantom image (without noise)

| Reconstruction methods | RRMSE | SI | SSIM |
|---|---|---|---|
| FBP | 0.1282 | 44.9556 | 0.6110 |
| ART [6] | 0.1120 | 25.5737 | 0.7681 |
| SART [71] | 0.1198 | 25.0023 | 0.7663 |
| TV | 0.0715 | 20.0115 | 0.8716 |
| Proposed method | 0.0609 | 18.0646 | 0.9310 |

The reconstructions for head image are shown in Figure 4.7. Similar to the results of nodule phantom, the FBP reconstruction has serious undersampling and streaking artifacts, which are distributed over the whole image. With such few views of data, ART and SART can't produce diagnostically satisfactory images, showing artifacts in the brain areas, which might minic diseases features. We can see from Figure 4.7(e) that the brain areas are smooth in the TV reconstruction. But TV methods tends to oversmooth the image, making the soft tissue between bones difficult to recognize. TV also makes the skull look thicker than the original image. By contrast, the proposed algorithm is able to preserve these small tissue areas, leading to a better result. To quantify the reconstruction accuracy, the RRMSE, SI and SSIM values of the reconstructions are also shown in Table 4.3.

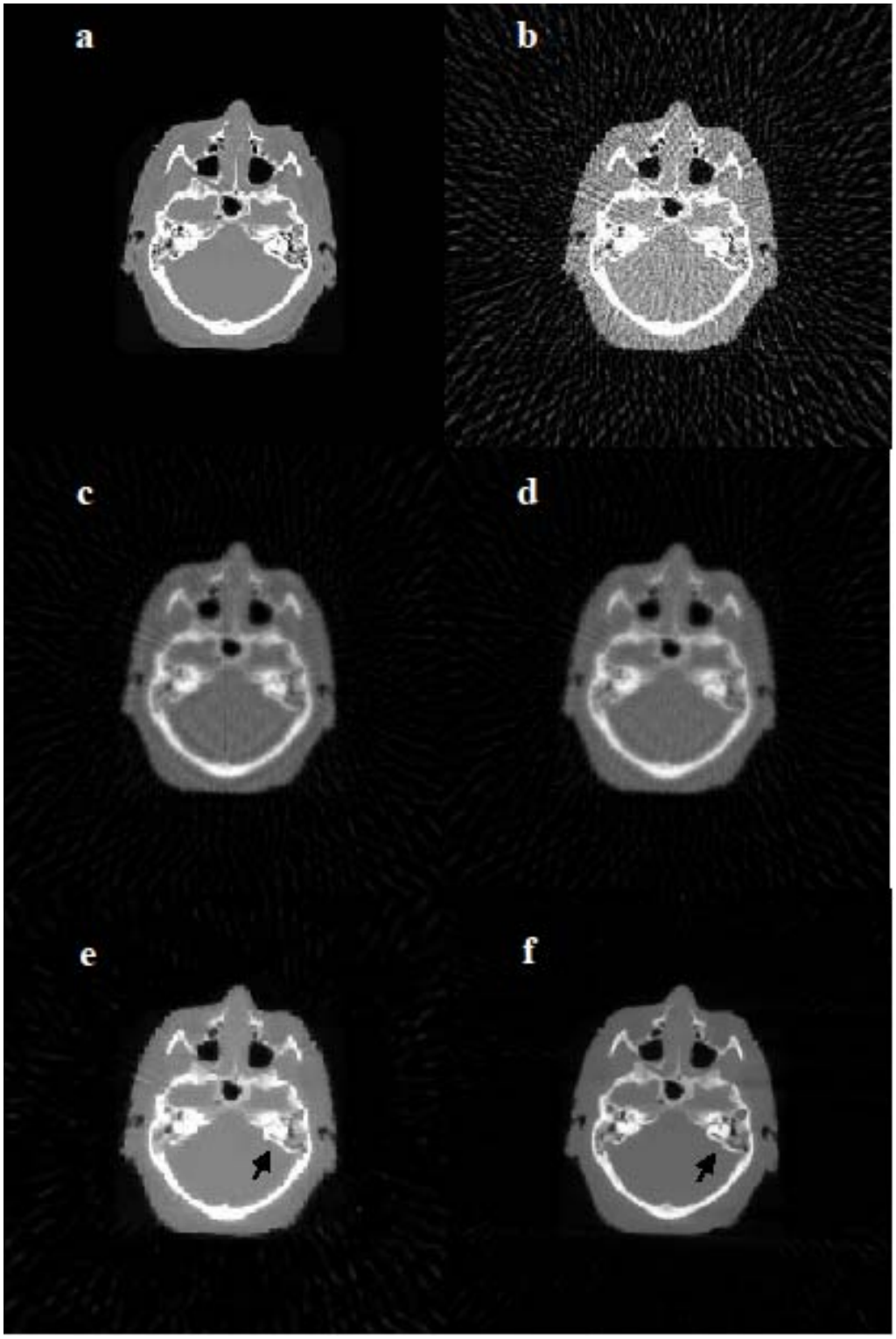


Figure 4.7 The reconstruction results of the head image using 50 views. (a) The ground truth image reconstructed with 1080 views, (b) the result obtained using FBP algorithm, (c) the ART algorithm, (d) the SART algorithm, (e) the TV algorithm, and (f) the proposed CS algorithm.

Table 4.3 Reconstruction results with 50 views using head image (without noise)

| Reconstruction methods | RRMSE | SI | SSIM |
|---|---|---|---|
| FBP | 0.3509 | 33.7287 | 0.3769 |
| ART [6] | 0.1965 | 17.4079 | 0.5753 |
| SART [71] | 0.1966 | 16.2995 | 0.5852 |
| TV | 0.1528 | 13.4362 | 0.7953 |
| Proposed method | 0.1212 | 11.5122 | 0.9099 |

## 4.5.2 Simulation with noise

The second experiment was performed using noisy simulated data. Additive Gaussian white noise $\mathbf{e}$ of relative magnitude $\|\mathbf{e}\|_2 / \|\mathbf{A}\boldsymbol{\mu}_{true}\|_2 = 0.05$ was purposely added to the sinograms. The results are displayed in Figure 4.8 and 4.9. To better compare the TV method and our proposed method, we also randomly selected one horizontal line intensity profile of the reconstructions of nodule phantom. The line intensity profiles are shown in Figure 4.10. Compared to FBP, ART is more robust to noise and thus have greatly suppressed the streaking artifacts. SART produces similar results (not shown in Figure 4.10). But there are high frequency vibrations around edges, as indicated by black arrows in Figure 4.10. The vibration is caused by the limited view (streak artifact) and noise added. The vibration is somehow eliminated in terms of frequency and amplitude in the TV reconstruction. This vibration may mimic low-contrast lesions, producing non-exist

structures. In contrast, the intensity profile of reconstructed image by the proposed method shows a rather smoothed curve in nonedge regions and is also much closer to the ground truth profile near edges, demonstrating its ability to produce better edges. The results are summarized in Table 4.4. It was evident that our algorithm showed strong robustness against noise.

Table 4.4 Reconstruction results with 50 views (with noise)

| Data | Reconstruction methods | RRMSE | SI | SSIM |
|---|---|---|---|---|
| Nodule phantom | FBP | 0.2908 | 127.465 | 0.3284 |
| | ART [6] | 0.1197 | 28.7409 | 0.7260 |
| | SART [71] | 0.1324 | 28.0063 | 0.7344 |
| | TV | 0.0891 | 24.1023 | 0.7693 |
| | Proposed method | 0.0687 | 21.2074 | 0.8967 |
| Head | FBP | 0.5375 | 48.6681 | 0.2271 |
| | ART [6] | 0.3021 | 38.9579 | 0.5016 |
| | SART [71] | 0.2979 | 26.5483 | 0.5279 |
| | TV | 0.1857 | 16.9268 | 0.7392 |
| | Proposed method | 0.1427 | 13.8576 | 0.8652 |

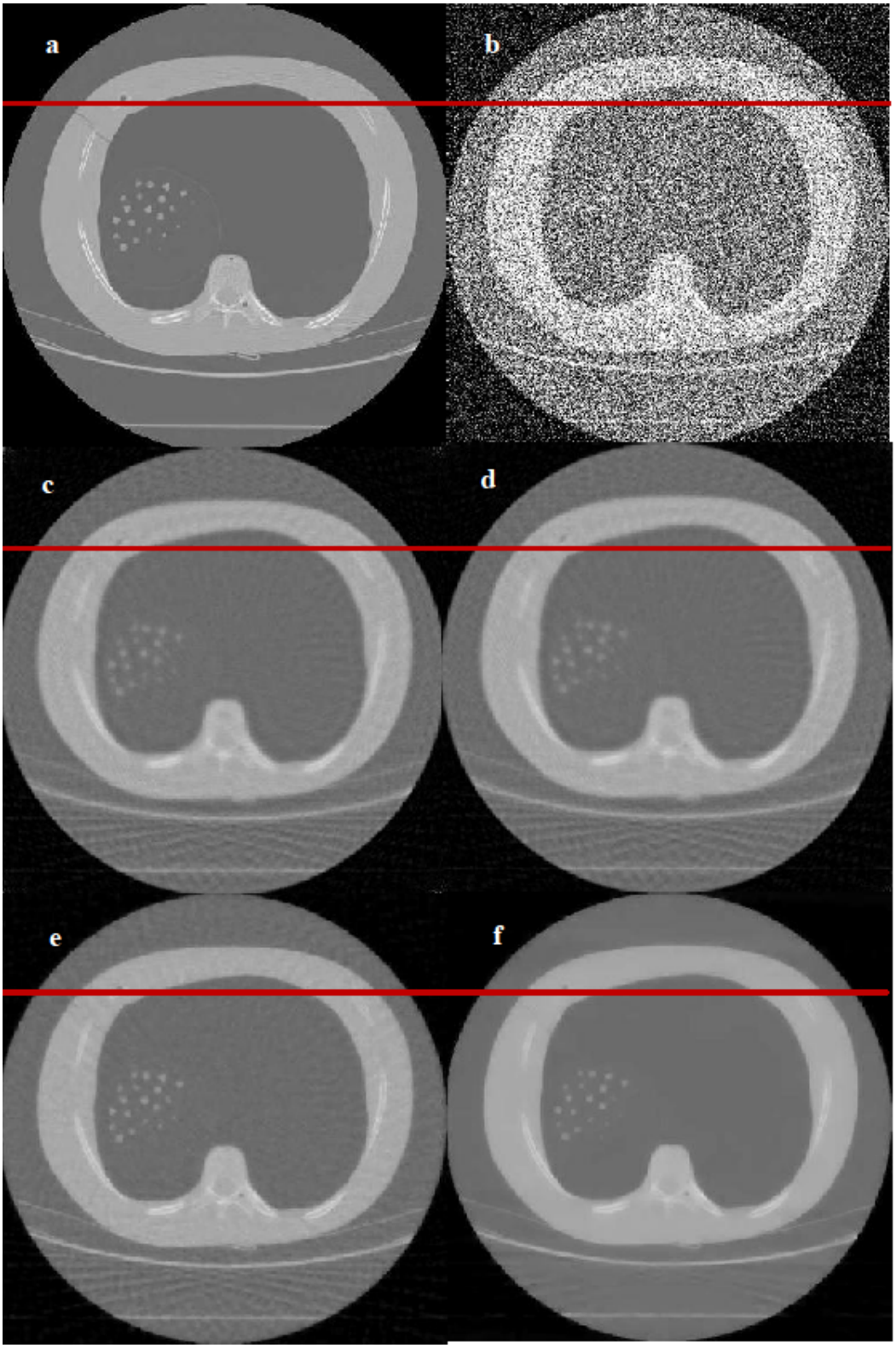


Figure 4.8: Simulated reconstruction of noisy phantom from 50 noisy projections over $180^0$: (a) the true image, (b) FBP, (c) ART, (d) SART, (e) TV, and (f) the proposed method.

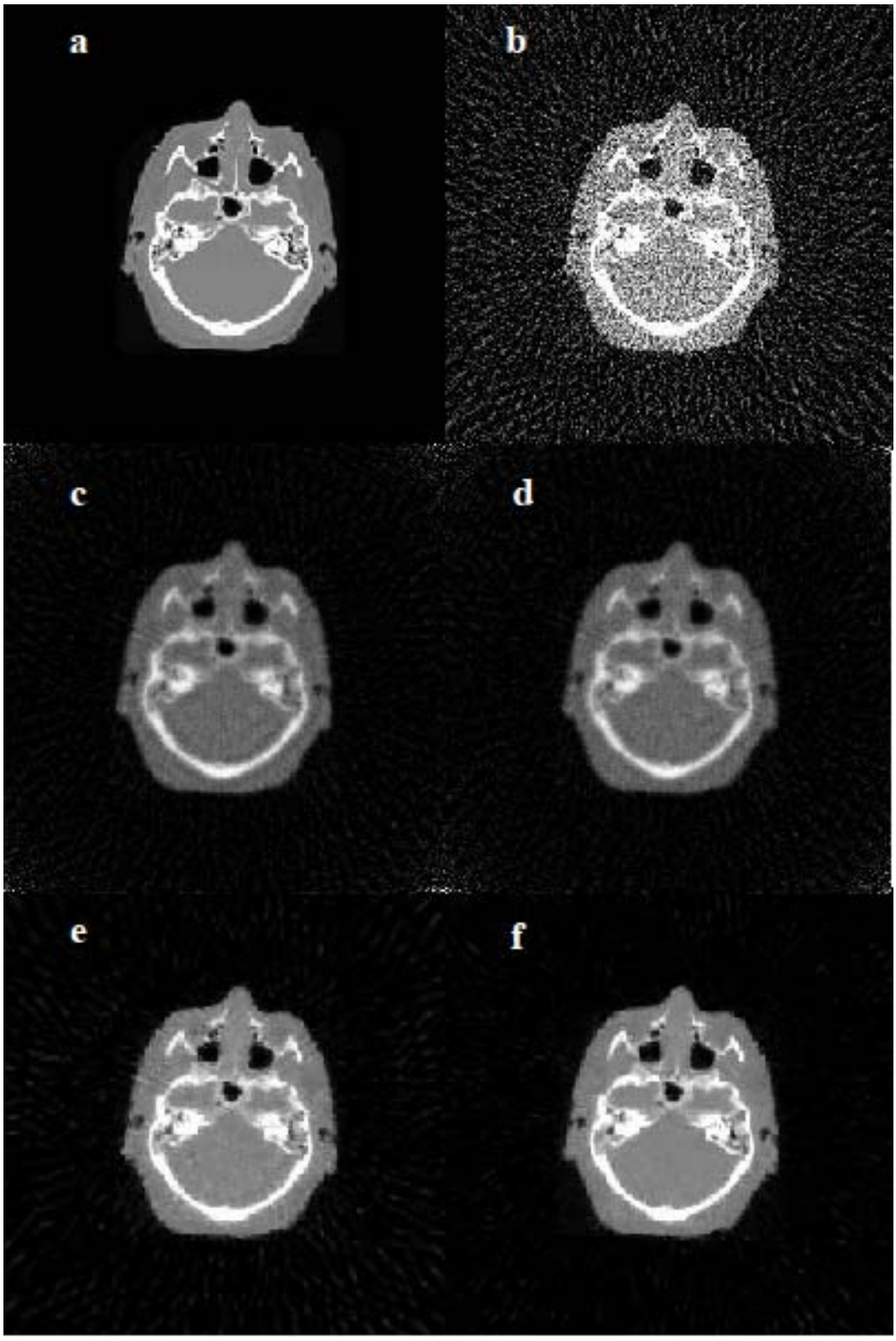


Figure 4.9: The reconstruction results of the head image from 50 noisy views. (a) The ground truth image, (b) the result obtained using FBP algorithm, (c) the ART algorithm, (d) the SART algorithm, (e) the TV algorithm, and (f) the proposed CS algorithm.

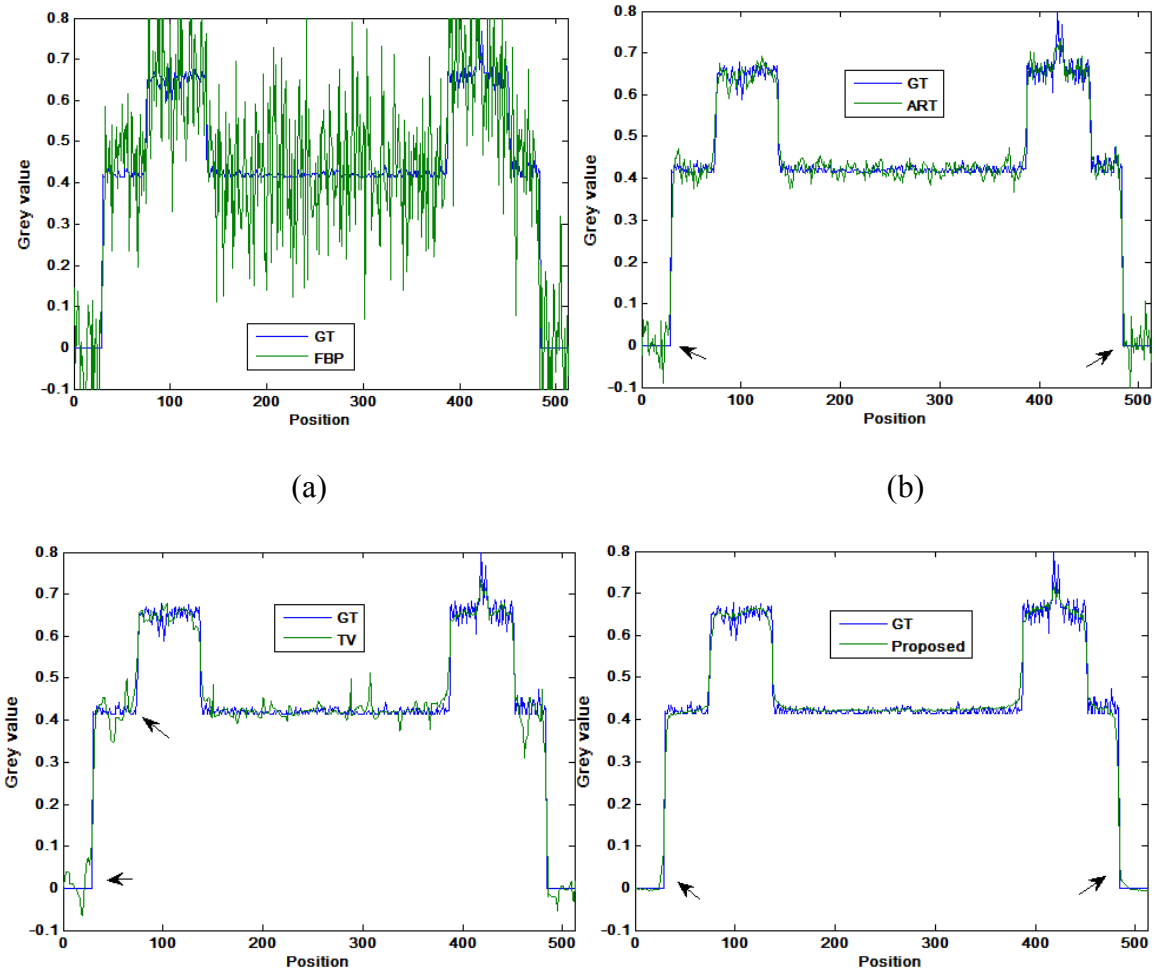


Figure 4.10: Pixel-intensity profiles of reconstructed phantom images compared with ground truth (GT): (a) FBP, (b) ART, (c) TV, and (d) the proposed method.

## 4.6 Experiment results using real projection data

In this section, we used real data collected from the Canadian Light Source facility and from a desktop Bruker SkyScan 1172 Micro-CT system with three datasets: human femoral cortical bone, the hindpaw of a normal Wistar rat and a human prostate. For the human bone, micro-CT scanning was performed at the BioMedical Imaging and Therapy

bending magnet beamline (BMIT-BM; 05B1-1) at the Canadian Light Source. Projections were collected with a Hamamatsu C9300 (Hamamatsu Photonics, Hamamatsu, Japan) CCD camera fitted with a beam monitor with a 10 μm thick gadolinium oxysulfide scintillator. The scans used the "white beam" method, filtering the x-ray beam with aluminum (6 mm) and tin (0.5 mm) foils to generate a peak x-ray energy intensity in the 25-29 keV energy range. The sample was rotated through $180^{o}$ at 0.1 degree steps, generating 1800 original projections. The image size is of 3780×3780 pixels, with 1.4 μm voxels. We selected a region of interest (ROI) from this image for demonstration of the different algorithms on the reconstructed images. The FBP reconstruction using the full 1800 projections is shown in Figure 4.11(a).

The second dataset in this study was a microCT scan of an adult Wistar rat hindpaw. This scan was taken at 70 kVp with the Bruker SkyScan 1172 Micro-CT in Anatomy & Cell Biology at the University of Saskatchewan. The reconstructed pixel size was 26.6 um. In total, 900 projections were acquired over a rotation through $180^{o}$ at 0.2 degree steps. The FBP reconstruction using these full 900 projections is shown in Figure 4.11(b). The optimum parameter selections for real data set are shown in Table 4.5.

The last dataset in this thesis was a CT scan of a human prostate at the Canadian Light Source. The FBP reconstruction using 3750 projections was used as the reference image.

Reduced data sets were obtained by equally skipping the projection data from the full

data sets.

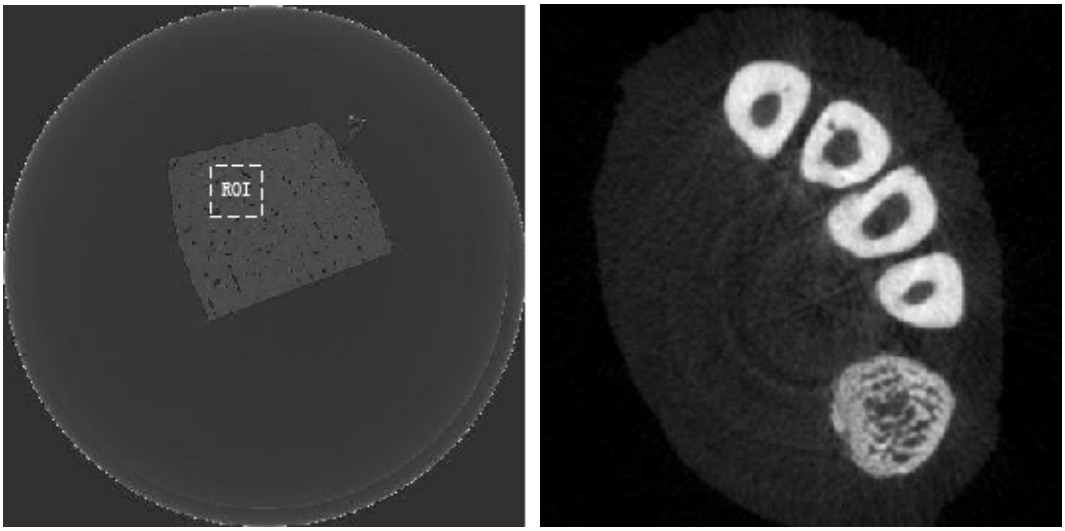


(a) (b)

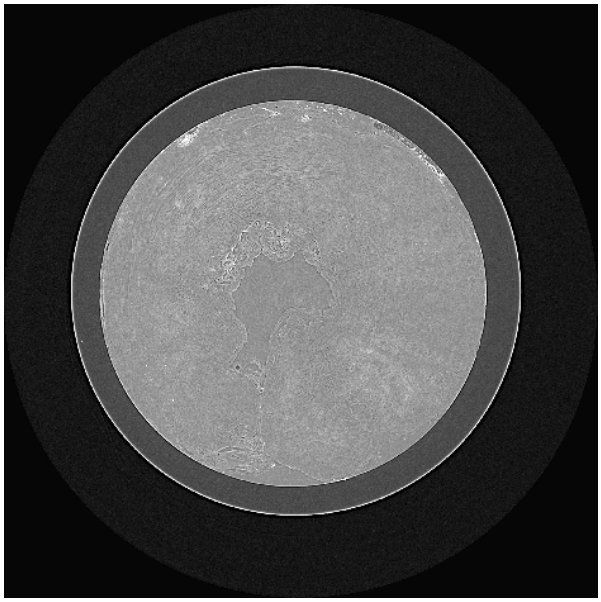

(c)

Figure 4.11: Reference images obtained from the complete dataset. (a) Human bone. (b) Rat hindpaw. (c) Human prostate. The human bone image has a large smooth region, so to better demonstrate the details, a region of interest (ROI) is selected.

Table 4.5: Optimum parameter selections for real data sets

| Data | TV algorithm | Proposed algorithm | |
|---|---|---|---|
| | $\lambda$ | $\lambda_1$ | $\lambda_2$ |
| Human bone | 0.001 | 0.001 | 0.001 |
| Rat | 0.0005 | 0.001 | 0.0005 |
| Prostate | 0.0008 | 0.0012 | 0.0007 |

The ROI reconstruction results restricted to 50-views for the human cortical bone image are shown in Figure 4.12. The gray tissue shown is the bone permeated with vascular canals, which appear darker in the image. Surrounding these larger canals some smaller objects can be seen. These are osteocyte lacunae, spaces within the bone where cells reside. The edges of the canals and lacunae are highlighted by propagation phase contrast halos.

As expected the limited view FBP reconstruction shows a greater amount of high spatial frequency noise over the entire area due to the limited sampling rate. The resolution is significantly diminished and many details of interest including the lacunae are lost. Image quality is lowered with strong and obvious streaking artifacts. In the ART and SART images, the streaking artifacts and noise are reduced, but residual artifacts can be seen and the noise is still pervasive. Besides this, they suffer from edge blurring artifacts and many low-contrast structures are lost. The edges of the vascular canals are no longer able to be precisely distinguished, an important feature for characterizing their

shape and size. The streaking artifacts in the TV reconstruction are less conspicuous than they are in FBP, ART and SART, but we can clearly see some relatively low frequency patchy structures present in non-edge regions. In clinical practice, these patchy structures may minic low-contrast lesions and obscure the presence of small details. By comparison, our proposed method provides reconstruction of high fidelity, as presented in Figure 4.12(f). It is able to remove most of the streak artifacts without visible introduction of unwanted structures. For instance, the canals in the bone are much clearer in the image reconstructed by our proposed method than that in the image reconstructed by TV method, that their edges are much cleaner. This ROI, which contains many fine structures, demonstrates the ability of our proposed algorithm to preserve fine details and structures while suppressing streaking artifacts.

To further quantify the reconstruction accuracy and streaking artifacts, the RRMSEs, SIs and SSIMs values of the given ROI by these methods are shown in Table 4.6. From the table, we can see that the RRMSE is well below 10% for both TV and our proposed method with the latter showing superior results. This results indicates that high reconstruction accuracy can be achieved using our proposed method. As well, from the SI value and visual observation of Figure 4.12, one may conclude that the proposed algorithm is capable of greatly suppressing streaking artifacts and noise, leading to an image of acceptable quality at a greatly reduced number of views.

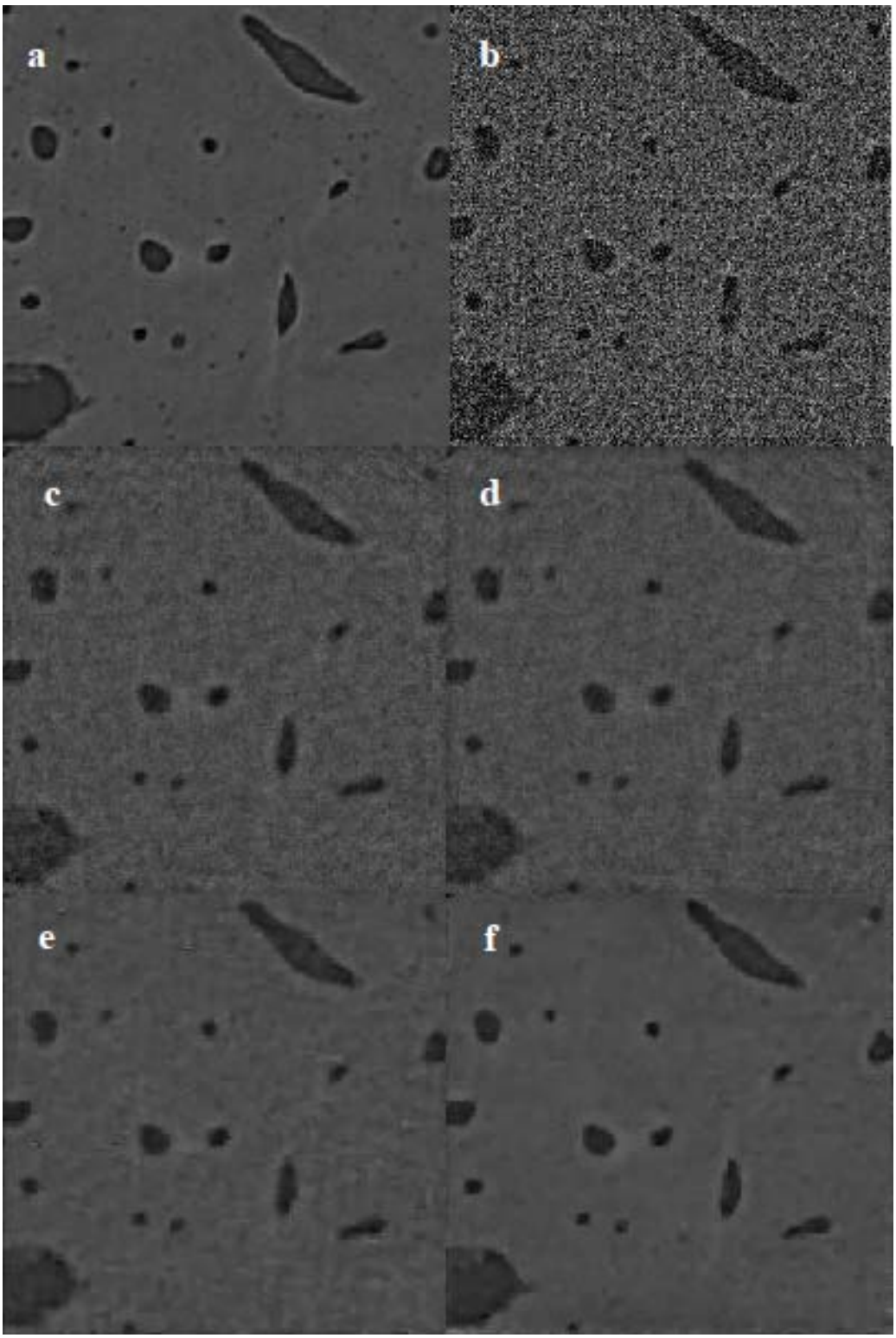

Figure 4.12: The ROI reconstructions of human bone. (a)The image reconstructed by FBP with 1800 projections, (b) the result obtained using FBP algorithm, (c) the ART algorithm, (d) the SART algorithm, (e) the TV algorithm, and (f) the proposed CS algorithm, all using 50-views.

Table 4.6 Reconstruction results with 50 views using human bone data set

| Reconstruction methods | RRMSE | SI | SSIM |
|---|---|---|---|
| FBP | 0.5102 | 97.325 | 0.3040 |
| ART [6] | 0.1525 | 22.9236 | 0.6893 |
| SART [71] | 0.1412 | 20.0544 | 0.6955 |
| TV | 0.0783 | 6.7528 | 0.7983 |
| Proposed method | 0.0557 | 4.1120 | 0.8642 |

Now let us look at the adult Wistar rat hindpaw image. This image shows a transverse slice through the bones of the paw, with the bottom bone showing trabecular bone and the other four bones showing cortical bone and marrow cavities. The experimental results of the rat are displayed in Figure 4.13.

Image quality is greatly degraded by obvious streaking artifacts in FBP reconstruction due to its inability to handle incomplete data. These artifacts are not efficiently removed by either ART or SART algorithms. By comparison, image reconstructed by the TV method and proposed method appear to have higher visual image quality, indicating that TV-based methods are superior to these methods. Although the TV method can suppress the noise and streak artifacts considerably, it is still a great challenge to reconstruct the trabecular bone, the fine structure in the bottom right-hand corner of the image as indicated by the red arrows in Figure 4.13(e), because of the nature of total variation regularization. By the introduction of the wavelet transform in image reconstruction procedure, our proposed method minimizes noise and streaking artifacts both in the

discrete gradient domain and wavelet domains, delivering better results than previous efforts without creating unwanted smoothing effects. Our method leads to a better reconstruction with higher spatial resolution.

For a comprehensive comparison, the RRMSEs, SIs and SSIMs of the reconstructed images are also plotted against the number of projections in Figure 4.14 (a), (b) and (c), respectively. The shape of the curves shows the effectiveness of the corresponding reconstruction method in sparse-view regime. The relative error decreases significantly as the number of projections increases from 20 to 50. Figure 4.14 indicates that RRMSEs, SIs of reconstructions by the proposed method in all cases are lower than those of other methods while the SSIMs are higher than those of other methods. The results of this test confirm that the proposed method outperforms the TV method in maintaining the balance between noise suppression and spatial resolution preservation.

Finally, we will look at the results of human prostate. The reconstructed images for 50 views are displayed in Figure 4.15. The top right corner shows the detailed view of the image. For the FBP reconstruction in Figure 4.15(b), the streaking artifacts and noise make it impossible to tell whether it is noise or some structures, see the zoom-in at the top right corner of (b). Although ART and SART can greatly remove the streaking artifacts, the images are blurred. In the zoom-ins, we can not see any structures. From Figure 4.15(e) and (f), we can see that the streaking artifacts and aliasing artifacts are significantly suppressed by compressed sensing. But from the zoom-ins, we can see that

the reconstructed image by the proposed method has more visible small canals. The edges are more clear in (f) than (e). Table 4.7 shows the RRMSE, SI and SSIM of the results. From the table, we also confirm that the proposed method outperforms the others.

The reconstructed images by the proposed method from 100, 150 and 180 views are shown in Figure 4.16 to demonstrate the ability of the proposed method. From Figure 4.16(d), we can see from the zoom that, the proposed method can provide nearly perfect reconstruction using 180 views. The canals can be clearly seen. But the number of projections is only 180, which is $\frac{180}{3750}\times 100\% = 4.8\%$ of the data used by the original image. Theoretically, the radiation dose will be simply reduce by 3750/180=20.83 times. This huge reduction of radiation dose can be of great benefit for clinical application.

## 4.7 Discussion

The assumption of compressibility is critical for all compressed sensing based methods, including the proposed method. Fortunately, medical images are found to be compressible in some transform domains [52]. Although previous work has found total variation to be a very effective, robust, and simple method, some articles found it may lead to unwanted smoothing effects and "blocky" effects [24, 72]. In contrast, the method presented in this study combines total variation and the discrete wavelet transform, the latter of which has been studied for decades and is widely used for image compression [73, 74].

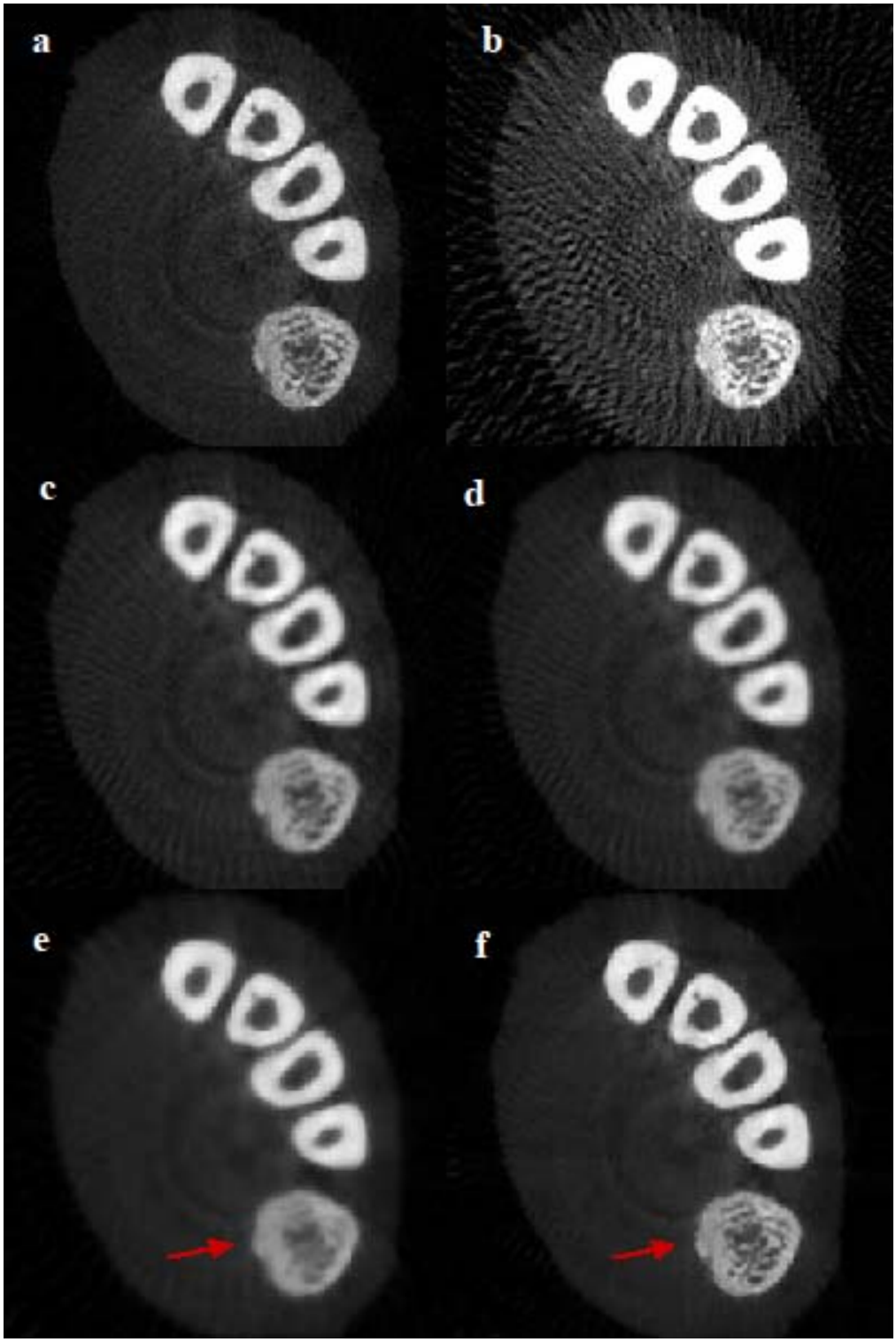


Figure 4.13: Reconstruction results of the hindpaw image of the adult rat. (a) FBP reconstruction using 900 projections, (b) FBP algorithm with 50 projections, (c) ART algorithm, (d) SART algorithm, (e) TV algorithm, and (f) the proposed CS algorithm, all using 50 views.

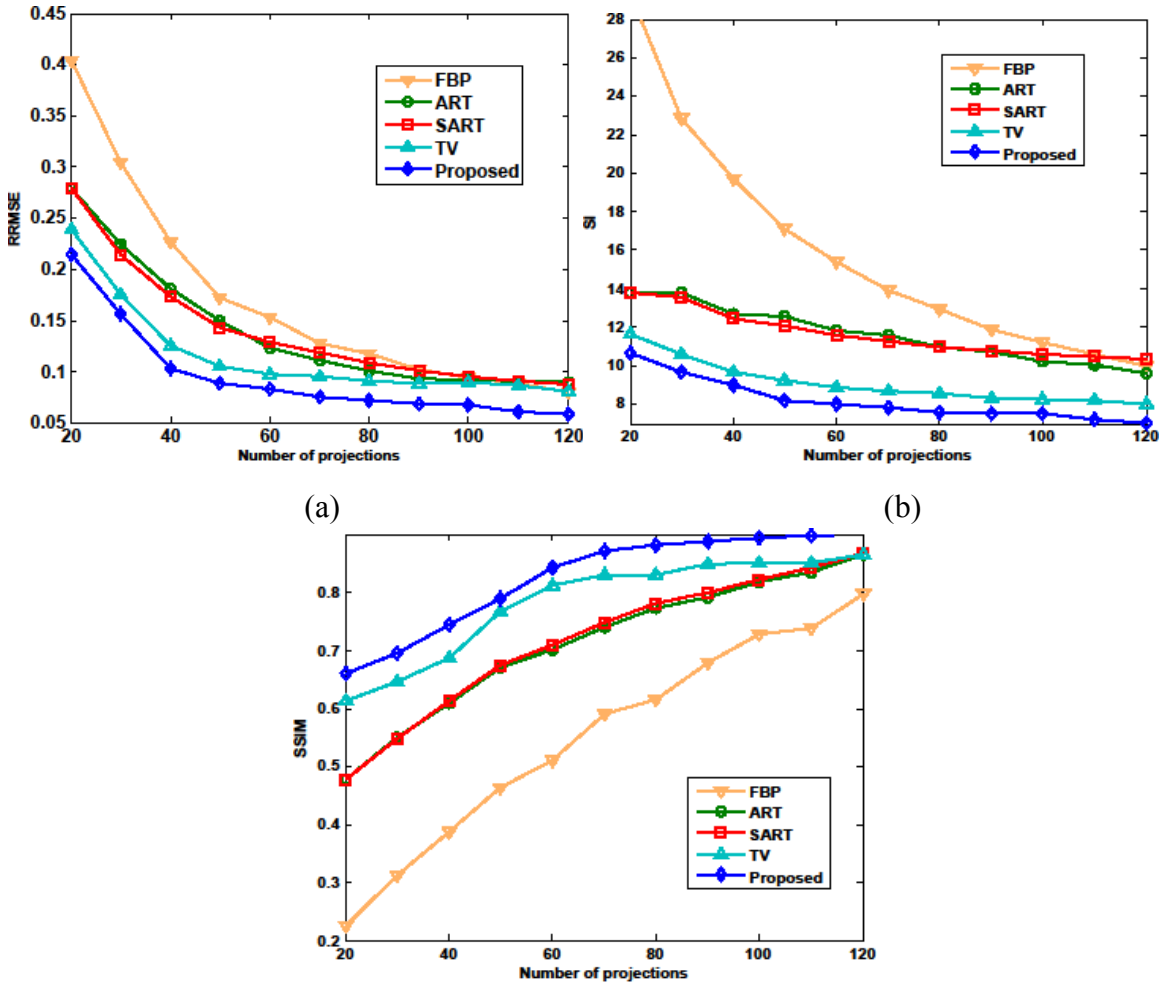


Figure 4.14: Plots of relative root mean square error (RRMSE), streak indicator (SI), and structural similarity (SSIM) for rat dataset.

Table 4.7 Reconstruction results with 50 views using human prostate data set

| Reconstruction methods | RRMSE | SI | SSIM |
|---|---|---|---|
| FBP | 0.3999 | 456.26 | 0.5314 |
| ART [6] | 0.1724 | 134.95 | 0.6755 |
| SART [71] | 0.1739 | 134.36 | 0.6784 |
| TV | 0.1412 | 123.62 | 0.7285 |
| Proposed method | 0.1186 | 111.26 | 0.8037 |

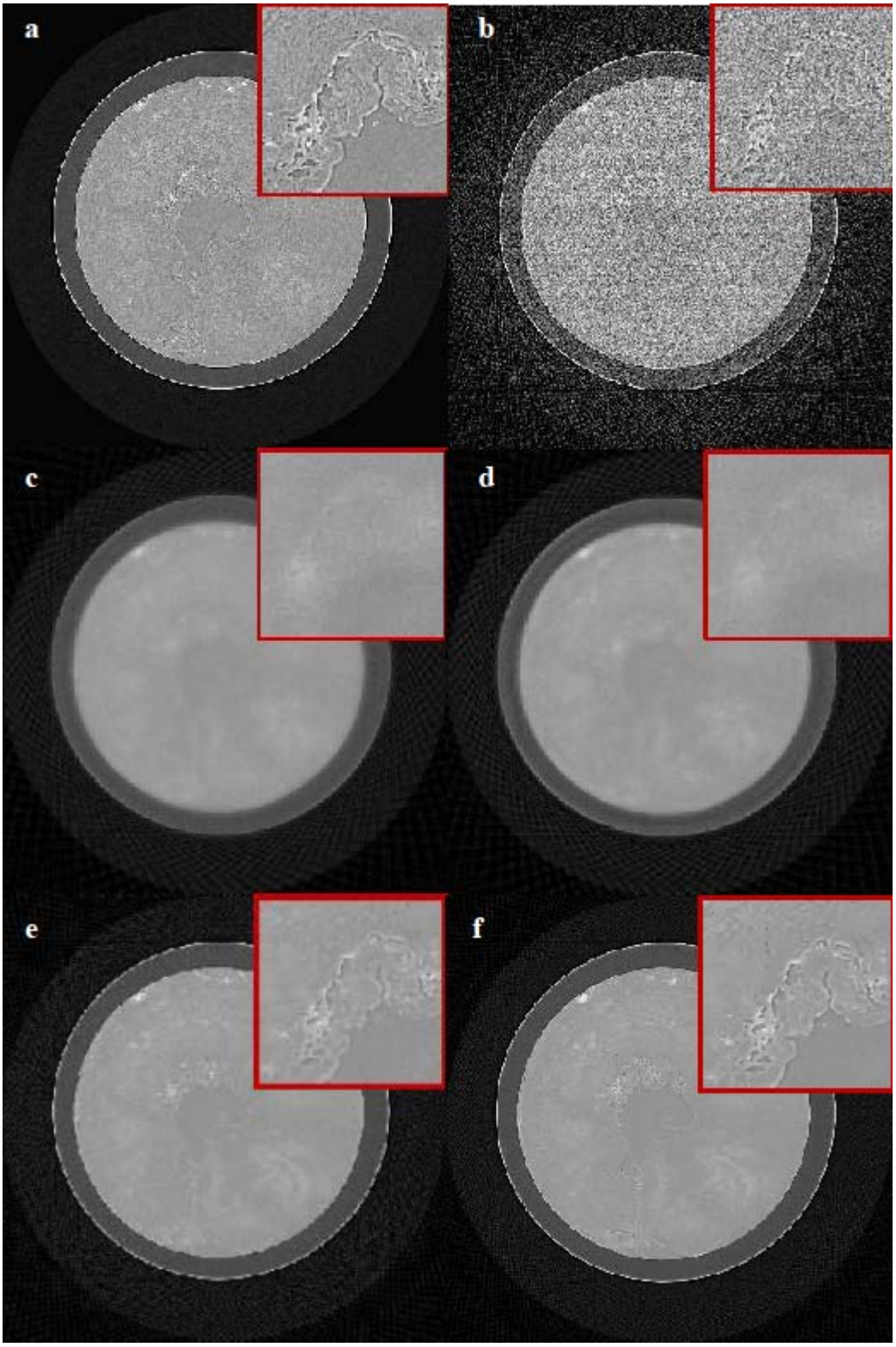


Figure 4.15: Reconstruction results of human prostate. (a) FBP reconstruction using 3750 projections, (b) FBP algorithm with 50 projections, (c) ART algorithm, (d) SART algorithm, (e) TV algorithm, and (f) the proposed CS algorithm, all using 50 views.

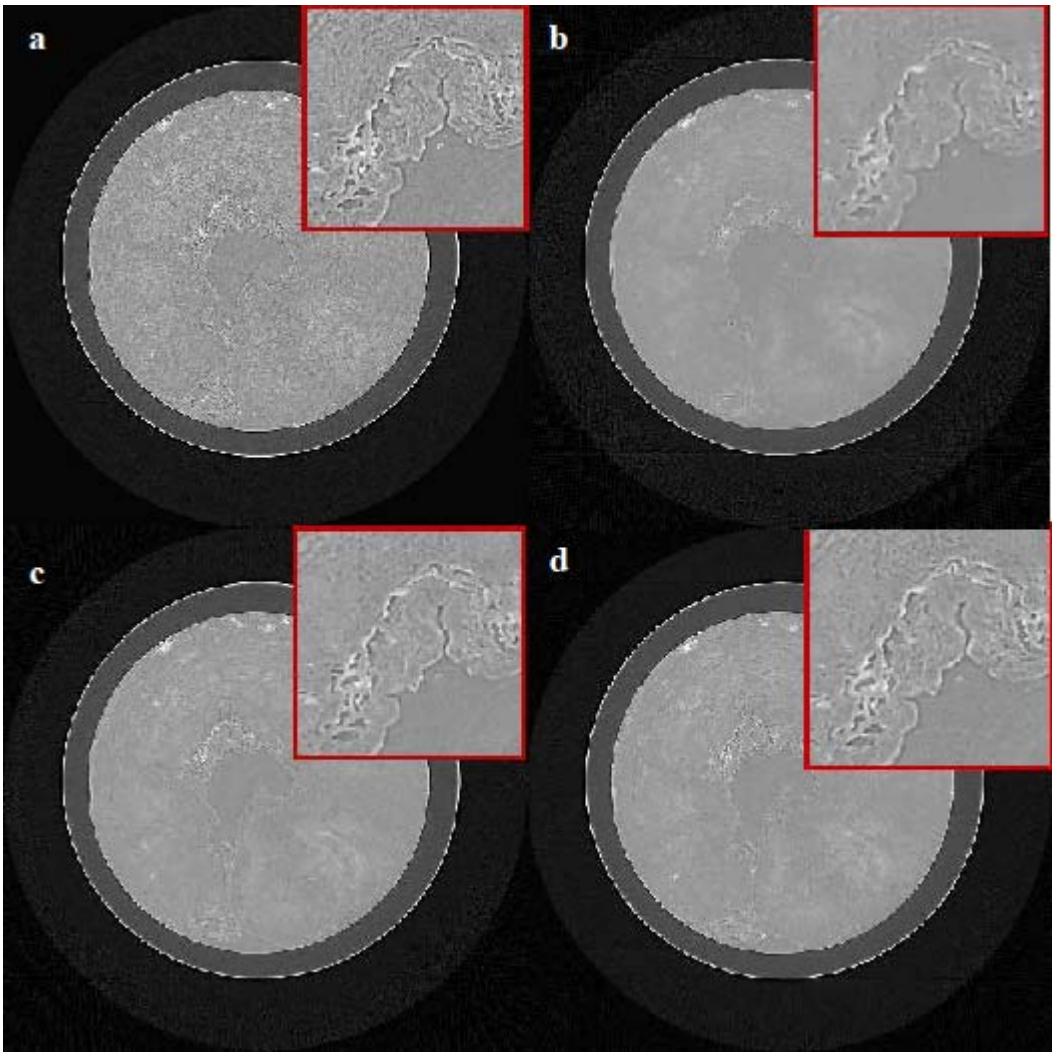


Figure 4.16: Reconstruction results of human prostate by the proposed method. (a) Reference image by FBP reconstruction using 3750 projections, CS reconstructions from (b) 100 views, (c) 150 views, (d) 180 views.

As a result, streaking artifacts and noise are minimized in two transform domains, being capable of suppressing streak artifacts and preserving fine structures.

Medical imaging both at the clinical level and in research has great demand for CT scans that take less time and receive less dose. Clinical CT and in vivo research micro-CT

scans rely on speed to avoid movement artifacts produced by small involuntary patient movements including those produced by respiration and cardiac motion. They are also limited by the amount of radiation dose produced at high resolution. Because resolution scales exponentially with dose, any reduction in the number of projection images required for accurate reconstruction will assist in the development of more advanced in vivo micro-CT protocols and more accurate diagnostic CT imaging.

The convergence speed of an algorithm is a crucial factor for all iterative methods in clinical practice. To investigate the convergence speed of the proposed method, plot of cost function value $J(\boldsymbol{\mu})$ in equation (4.1) against the number of of iterations for the phantom dataset (without noise) is shown in Figure 4.17 with 30-views selected for demonstration. Figure 4.17 shows that the curve decreases dramatically within 5 iterations, indicating the high convergence speed of our proposed method. One should also note that TV method can produce accurate reconstructions given enough iterations. In the comparative study in this thesis, we use the same number of iterations for TV and our method to produce an unbiased comparison. This shows that not only is our method superior to TV method in terms of reconstruction accuracy, streaking artifacts and structural similarity, but also in terms of convergence speed.

All experiments were conducted on a Lenovo computer with Intel(R) Xeon(R) CPU E5-2620 @ 2.00GHz and 32GB DDR memory. The computation times for the rat dataset in the case of 50 projections are shown in Table 4.8. Although TV method and proposed

method can produce high quality of images, the computation times are much higher than other methods. As a result, there is tradeoff between reconstruction accuracy and efficiency.

Table 4.8 Reconstruction time for the rat dataset in case of 50 views

| | FBP | ART | SART | TV | Proposed |
|---|---|---|---|---|---|
| Time (s) | 4 | 347 | 9 | 928 | 925 |

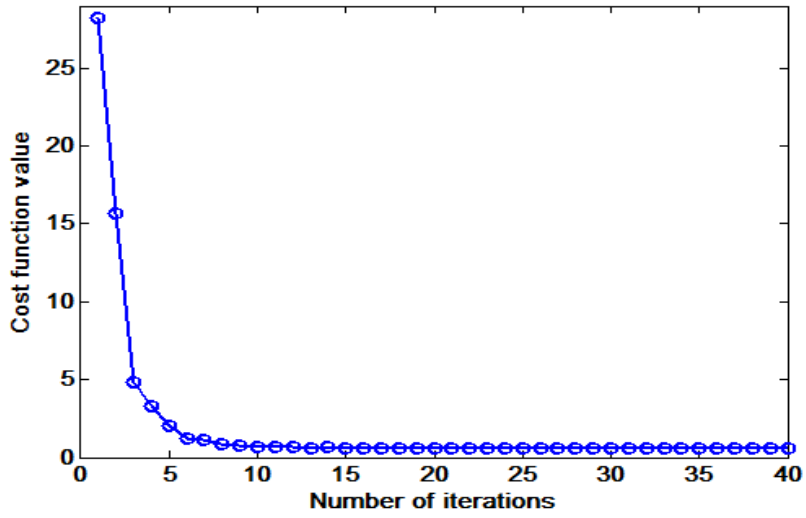


Figure 4.17: Convergence curve (cost function values versus number of iterations) for the proposed method applied to phantom dataset.

## 4.8 Conclusion

In this chapter, we have investigated a novel compressed sensing-based algorithm for

sparse-view CT image reconstruction, in which wavelet transform is used in the reconstruction procedure. Results show that the proposed method is able to suppress streak artifacts and noise caused by incomplete and noisy projection data without visible oversmoothing of fine structure details in the images. The proposed CS based algorithm has potential to reduce the dose in clinical computed tomography imaging techniques.

# Chapter 5

# Conclusions and future work

In this thesis, we aimed to reduce the required X-ray radiation dose in CT imaging and potentially the amount of radiation absorbed by patients during CT examinations. Currently, the defacto standard for image reconstruction on the commercial CT scanners are based on densely sampled projections over the scanning angular range. Therefore, huge projection data are obtained in order to get a high quality of image. In fact, the traditional FBP algorithm, ART or SART algorithms are guaranteed to produce acceptable images if the number of projections is very high. However, this high radiation exposure may induce cancer later in life. In addition, the resolution and image quality of micro-CT are also restricted by radiation dose. Therefore, methods to suppress degradation due to non-sufficient measurements are of great interest to the CT community. In particular, compressed sensing has attracted significant interest since it can greatly improve image quality using highly incomplete data.

Compressed sensing requires the image of interest to be approximately sparse in order to recover images from few samples. Fortunately, it is easy to fulfill this requirement by transform coding: most medical images can be compressed by a variety of transforms e.g., wavelet, DCT, etc. In particular, the image gradient transform, also known as TV, is popular in compressed sensing CT because minimizing the image gradient will efficiently

suppress streak artifacts, aliasing artifacts and noise. But TV based compressed sensing methods are poor at reconstructing edges and small features. In this thesis, we developed an improved compressed sensing based method for CT image reconstruction. To summarize, this thesis involves:

- a review of CT imaging and traditional image reconstruction algorithms
- a review of compressed sensing
- a review of existing compressed sensing base CT imaging algorithms
- the improved compressed sensing algorithm for CT image reconstruction

The major contribution of this thesis is the proposed improved algorithm for higher quality image reconstruction. In the proposed algorithm, we simultaneously minimize the ℓ1 norm, total variation and a least squares measure. Particularly, wavelet transform is employed as the sparsity transform because it is good at capturing point singularities. As a result, through controlling the parameters, we may simultaneously suppress artifacts and preserve small features. In Chapter 4 of this thesis, we introduced our proposed algorithm. We proposed to solve the minimization problem using one of the best nonlinear conjugate gradient methods. Several experiments using simulated projection data and real data have demonstrated the effectiveness of the proposed method. It can be concluded as follows.

FBP and ART based methods can produce acceptable quality of images only when

they are provided sufficient projection data, typically, 1000-3000 views of data for high resolution CT images. But ART based methods outperform FBP when noisy data or slightly incomplete data is used. But when data is high incomplete, the image quality by these methods will degrade significantly. On the other hand, compressed sensing based methods are able to great improve the image quality. Even still, it remains great challenge for the existing TV based compressed sensing methods to reconstruct small objects. The proposed method is able to solve this problem by combining two transforms. The results presented in this thesis indicate the ability of the proposed method. One of the application for the proposed algorithm is to reduce the time to scan the patient because lower number of projections is needed for reconstruction. Also, since the radiation dose is reduce, it becomes more safety to have a CT examination.

The major drawback of our proposed method is the long computational time. Typically, it takes several minutes to reconstruct a 256×256 image. The development of GPU implementation will be one of the future works. The other future direction is exploiting more efficient iterative algorithm to solve the minimization problem. Finally, more research need to be done on how to apply this technique to clinical data. When we extend to clinical application, we need to synthesize the sampling patter into the CT system.

# Papers published by author

1. **Zangen Zhu**, Khan Wahid, Paul Babyn, David Cooper, Isaac Pratt, Yasmin Carter, "Improved compressed sensing-based algorithm for sparse-view CT image reconstruction." *Computational and Mathematical Methods in Medicine,* vol. 2013, 2013, 15 pages. [PDF]
2. **Zangen Zhu**, Khan Wahid, Paul Babyn, Ran Yang, " Compressed Sensing based MRI Reconstruction using Complex Double-Density Dual-Tree DWT." *International Journal of Biomedical Imaging,* vol. 2013, 2013, *12* pages. [PDF]
3. Varun Gopi P, **Zangen Zhu**, Palanisamy. P, Khan Wahid, Babyn, "Iterative method for CT image reconstruction from reduced number of projection views." *Electrical & Computer Engineering (CCECE), 2013 26th IEEE Canadian Conference on, 2013.* [IEEE]
4. **Zangen Zhu**, Khan Wahid, Paul Babyn, "CT image reconstruction from partial angular measurements via compressed sensing," in *Electrical & Computer Engineering (CCECE), 2012 25th IEEE Canadian Conference on*, 2012, pp. 1-4. [IEEE]
5. **Zangen Zhu**, Khan Wahid, Paul Babyn, "CT image reconstruction from few views via compressed sensing," in *Information Science, Signal Processing and their Applications (ISSPA), 2012 11th International Conference on*, 2012, pp. 1428-1429. [IEEE]
6. **Zangen Zhu**, Ran Yang, Jingxin Zhang, Cishen Zhang, "Compressed sensing MRI by

two-dimensional wavelet filter banks," in *Multidimensional (nD) Systems (nDs), 2011 7th International Workshop on*, 2011, pp. 1-6. [IEEE]

# Bibliography


[1] A. M. Cormack, "Representation of a function by its line integrals, with some radiological applications," *Journal of Applied Physics,* vol. 34, pp. 2722-2727, 1963.

[2] G. N. Hounsfield, "Apparatus for examining a body by radiation such as X or gamma radiation," ed: Google Patents, 1976.

[3] G. T. Herman*, et al.*, "ART: Mathematics and applications: a report on the mathematical foundations and on the applicability to real data of the algebraic reconstruction techniques," *Journal of theoretical Biology,* vol. 42, pp. 1-32, 1973.

[4] R. Gordon, "A Tutorial on ART (Algebraic Reconstruction Techniques," *IEEE Trans. Nucl. Sci. NS-21,* pp. 78-93, 1974.

[5] R. Gordon*, et al.*, "Algebraic reconstruction techniques (ART) for three-dimensional electron microscopy and X-ray photography," *Journal of theoretical Biology,* vol. 29, pp. 471-481, 1970.

[6] S. Kaczmarz, "Angenäherte auflösung von systemen linearer gleichungen," *Bulletin International de l'Academie Polonaise des Sciences et des Lettres,* vol. 35, pp. 355-357, 1937.

[7] A. Kak and M. Slaney, *Principles of Computerized Tomographic Imaging*. New York: IEEE Press, 1988.

[8] A. Andersen and A. Kak, "Simultaneous algebraic reconstruction technique

(SART): a superior implementation of the ART algorithm," *Ultrasonic imaging,* vol. 6, pp. 81-94, 1984.

[9] G. Wang and M. Jiang, "Ordered-subset simultaneous algebraic reconstruction techniques (OS-SART)," *Journal of X-ray Science and Technology,* vol. 12, pp. 169-177, 2004.

[10] H. Yu and G. Wang, "SART-type image reconstruction from a limited number of projections with the sparsity constraint," *Journal of Biomedical Imaging,* vol. 2010, p. 3, 2010.

[11] E. Hall and D. Brenner, "Cancer risks from diagnostic radiology," *British Journal of Radiology,* vol. 81, pp. 362-378, 2008.

[12] A. Berrington de Gonzalez*, et al.*, "Projected cancer risks from computed tomographic scans performed in the United States in 2007," *Archives of internal medicine,* vol. 169, p. 2071, 2009.

[13] D. J. Brenner and E. J. Hall, "Computed tomography—an increasing source of radiation exposure," *New England Journal of Medicine,* vol. 357, pp. 2277-2284, 2007.

[14] Z. Tian*, et al.*, "Low-dose CT reconstruction via edge-preserving total variation regularization," *Physics in Medicine and Biology,* vol. 56, p. 5949, 2011.

[15] D. L. Donoho, "Compressed sensing," *Information Theory, IEEE Transactions on,* vol. 52, pp. 1289-1306, 2006.

[16] Y. Tsaig and D. L. Donoho, "Extensions of compressed sensing," *Signal*

*processing,* vol. 86, pp. 549-571, 2006.

[17] E. J. Candès and M. B. Wakin, "An introduction to compressive sampling," *Signal Processing Magazine, IEEE,* vol. 25, pp. 21-30, 2008.

[18] E. J. Candès*, et al.*, "Robust uncertainty principles: Exact signal reconstruction from highly incomplete frequency information," *Information Theory, IEEE Transactions on,* vol. 52, pp. 489-509, 2006.

[19] W. B. Pennebaker and J. L. Mitchell, *JPEG: Still image data compression standard*: Kluwer Academic Pub, 1992.

[20] D. S. Taubman*, et al.*, "JPEG2000: Image compression fundamentals, standards and practice," *Journal of Electronic Imaging,* vol. 11, pp. 286-287, 2002.

[21] G.-H. Chen*, et al.*, "Prior image constrained compressed sensing (PICCS): a method to accurately reconstruct dynamic CT images from highly undersampled projection data sets," *Medical physics,* vol. 35, p. 660, 2008.

[22] E. Y. Sidky and X. Pan, "Image reconstruction in circular cone-beam computed tomography by constrained, total-variation minimization," *Physics in Medicine and Biology,* vol. 53, p. 4777, 2008.

[23] J. H. Jørgensen*, et al.*, "Accelerated gradient methods for total-variation-based CT image reconstruction," *arXiv preprint arXiv:1105.4002,* 2011.

[24] L. Ritschl*, et al.*, "Improved total variation-based CT image reconstruction applied to clinical data," *Physics in Medicine and Biology,* vol. 56, p. 1545, 2011.

[25] G. Herman and R. Davidi, "Image reconstruction from a small number of

projections," *Inverse Problems,* vol. 24, p. 045011, 2008.

[26] D. Donoho and X. Huo, "Combined image representation using edgelets and wavelets," *Wavelet Applications in Signal and Image Processing VII, in Proceedings SPIE,* vol. 3813, pp. 468-476, 1999.

[27] W. A. Kalender, *Computed Tomography: Fundamentals, System Technology, Image Quality, Applications*. Germany: Erlangen, 2005.

[28] J. Hsieh, *Computed tomography: principles, design, artifacts and recent advances*. Washington: SPIE Press, 2003.

[29] G. V. Gompel, "Towards accurate image reconstruction from truncated X-ray CT projections," University Antwerpen, Antwerpen, 2009.

[30] I. A. Elbakri, "Statistical reconstruction algorithms for polyenergetic X-ray computed tomography," The University of Michigan, 2003.

[31] H. P. Hiriyannaiah, "X-ray computed tomography for medical imaging," *Signal Processing Magazine, IEEE,* vol. 14, pp. 42-59, 1997.

[32] G. T. Gullberg*, et al.*, "Reconstruction algorithm for fan beam with a displaced center-of-rotation," *Medical Imaging, IEEE Transactions on,* vol. 5, pp. 23-29, 1986.

[33] L. Feldkamp*, et al.*, "Practical cone-beam algorithm," *JOSA A,* vol. 1, pp. 612-619, 1984.

[34] M. Defrise*, et al.*, "Rebinning-based algorithms for helical cone-beam CT," *Physics in Medicine and Biology,* vol. 46, p. 2911, 2001.

[35] T. M. Buzug, *Computed tomography: from photon statistics to modern cone-beam CT*: Springer, 2008.

[36] G. Herman, "Image reconstruction from projections," *Real-Time Imaging,* vol. 1, pp. 3-18, 1995.

[37] W. Zhen-Tian*, et al.*, "An ART iterative reconstruction algorithm for computed tomography of diffraction enhanced imaging," *Chinese Physics C,* vol. 33, p. 975, 2009.

[38] W. A. Kalender, *Computed tomography*: Publicis, 2011.

[39] J. F. Barrett and N. Keat, "Artifacts in CT: Recognition and avoidance1," *Radiographics,* vol. 24, pp. 1679-1691, 2004.

[40] S. Ma*, et al.*, "An efficient algorithm for compressed MR imaging using total variation and wavelets," in *Computer Vision and Pattern Recognition, 2008. CVPR 2008. IEEE Conference on*, 2008, pp. 1-8.

[41] B. K. Natarajan, "Sparse approximate solutions to linear systems," *SIAM journal on computing,* vol. 24, pp. 227-234, 1995.

[42] D. L. Donoho, "For most large underdetermined systems of linear equations the minimal 1-norm solution is also the sparsest solution" *Communications on pure and applied mathematics,* vol. 59, pp. 797-829, 2006.

[43] E. Candes and J. Romberg, "l1-magic: Recovery of sparse signals via convex programming," *URL: www. acm. caltech. edu/l1magic/downloads/l1magic. pdf,* vol. 4, 2005.

[44] E. J. Candes and T. Tao, "Decoding by linear programming," *Information Theory, IEEE Transactions on,* vol. 51, pp. 4203-4215, 2005.

[45] S.J. Kim*, et al.*, "An efficient method for compressed sensing," in *Image Processing, 2007. ICIP 2007. IEEE International Conference on*, 2007, pp. III-117-III-120.

[46] S. S. Chen*, et al.*, "Atomic decomposition by basis pursuit," *SIAM journal on scientific computing,* vol. 20, pp. 33-61, 1998.

[47] E. J. Candes and J. K. Romberg, "Signal recovery from random projections," in *Electronic Imaging 2005*, 2005, pp. 76-86.

[48] M. A. Figueiredo*, et al.*, "Gradient projection for sparse reconstruction: Application to compressed sensing and other inverse problems," *Selected Topics in Signal Processing, IEEE Journal of,* vol. 1, pp. 586-597, 2007.

[49] I. Daubechies*, et al.*, "An iterative thresholding algorithm for linear inverse problems with a sparsity constraint," *Communications on pure and applied mathematics,* vol. 57, pp. 1413-1457, 2004.

[50] R. Chartrand and W. Yin, "Iteratively reweighted algorithms for compressive sensing," in *Acoustics, Speech and Signal Processing, 2008. ICASSP 2008. IEEE International Conference on*, 2008, pp. 3869-3872.

[51] D. Needell, "Topics in compressed sensing," *arXiv preprint arXiv:0905.4482,* 2009.

[52] M. Lustig*, et al.*, "Sparse MRI: The application of compressed sensing for rapid

MR imaging," *Magnetic resonance in medicine,* vol. 58, pp. 1182-1195, 2007.

[53] S. O. Jin*, et al.*, "Bone-induced streak artifact suppression in sparse-view CT image reconstruction," *Biomedical engineering online,* vol. 11, pp. 1-13, 2012.

[54] X. Li*, et al.*, "A compressed sensing-based iterative algorithm for CT reconstruction and its possible application to phase contrast imaging," *Biomed Eng Online,* vol. 10, 2011.

[55] J. Jorgensen*, et al.*, "Ensuring convergence in total-variation-based reconstruction for accurate microcalcification imaging in breast X-ray CT," in *Nuclear Science Symposium and Medical Imaging Conference (NSS/MIC), 2011 IEEE*, 2011, pp. 2640-2643.

[56] M. E. Kilmer and D. P. O'Leary, "Choosing regularization parameters in iterative methods for ill-posed problems," *SIAM Journal on Matrix Analysis and Applications,* vol. 22, pp. 1204-1221, 2001.

[57] V. Agarwal, "Total Variation Regularization and L-curve method for the selection of regularization parameter," *ECE599,* 2003.

[58] M. Belge*, et al.*, "Efficient determination of multiple regularization parameters in a generalized L-curve framework," *Inverse Problems,* vol. 18, p. 1161, 2002.

[59] G.-H. Chen*, et al.*, "Prior image constrained compressed sensing (PICCS)," in *Proc Soc Photo Opt Instrum Eng*, 2008, p. 685618.

[60] Z. Zhu*, et al.*, "Improved Compressed Sensing-Based Algorithm for Sparse-View CT Image Reconstruction," *Computational and Mathematical Methods in*

*Medicine,* vol. 2013, 2013.

[61] J. Buckheit*, et al.*, "WaveLab Architecture," *URL: http://www-stat. stanford. edu/~ wavelab/Wavelab_850/WaveArch. pdf,* 1995.

[62] W. W. Hager and H. Zhang, "A survey of nonlinear conjugate gradient methods," *Pacific journal of Optimization,* vol. 2, pp. 35-58, 2006.

[63] E. K. Chong and S. H. Zak, *An introduction to optimization*: Wiley, 2013.

[64] S. Leng*, et al.*, "High temporal resolution and streak-free four-dimensional cone-beam computed tomography," *Physics in Medicine and Biology,* vol. 53, p. 5653, 2008.

[65] J. Tang*, et al.*, "Performance comparison between total variation (TV)-based compressed sensing and statistical iterative reconstruction algorithms," *Physics in Medicine and Biology,* vol. 54, p. 5781, 2009.

[66] Z. Wang*, et al.*, "Image quality assessment: From error visibility to structural similarity," *Image Processing, IEEE Transactions on,* vol. 13, pp. 600-612, 2004.

[67] National Cancer Institude: http://www.via.cornell.edu/databases/crpf.html

[68] National Library of Medicine: http://www.nlm.nih.gov/research/visible

[69] U. E. Ruttimann*, et al.*, "Statistical analysis of functional MRI data in the wavelet domain," *Medical Imaging, IEEE Transactions on,* vol. 17, pp. 142-154, 1998.

[70] K. Sidh*, et al.*, " Medical Image Denoising In The Wavelet Domain Using Haar And DB3 Filtering," *IRJES,* vol. 1, pp. 1-8, 2012.

[71] P. C. Hansen and M. Saxild-Hansen, "AIR Tools—A MATLAB package of

algebraic iterative reconstruction methods," *Journal of Computational and Applied Mathematics,* vol. 236, pp. 2167-2178, 2012.

[72] J. Song*, et al.*, "Sparseness prior based iterative image reconstruction for retrospectively gated cardiac micro-CT," *Medical physics,* vol. 34, p. 4476, 2007.

[73] Y. Jin*, et al.*, "Wavelets in medical image processing: denoising, segmentation, and registration," in *Handbook of biomedical image analysis*, ed: Springer, 2005, pp. 305-358.

[74] A. Manduca and A. Said, "Wavelet compression of medical images with set partitioning in hierarchical trees," in *Medical Imaging 1996*, 1996, pp. 192-200.